Quantum Optics and Photonics

Academic and Research Staff
Prof. Shaoul Ezekiel, Dr. Selim M. Shahriar, Dr. A. Kumarakrishnan, Dr. V. S. Sudarshanam, Dr. Alexey Turukhin, Dr. Parminder Bhatia, Dr. Venkatesh Gopal, Dr. DeQui Qing.

Visiting Scientist and Research Affiliates
Prof. Jeffrey Shapiro, Prof. Seth Lloyd, Prof. Cardinal Warde, Prof. Marc Cronin-Golomb, Dr. Philip Hemmer, Dr. Susanne Yelin, Dr. John Donoghue, Thomas Apel, John Kierstead

Graduate Students
Ying Tan, Jacob Morzinski, Thomas Liptay, Ward Weathers

Undergraduate Students
Aaron VanDevender, Shome Basu, Edward Flagg, Kathryn Washburn

Website: http://qop.mit.edu/

1. First Observation of Ultraslow Group Velocity of Light in a Solid

Sponsors: AFRL contract #F19628-00-C-0074 ARO grant #s DAAG55-98-1-0375 and DAAD19-001-0177, and AFOSR grant # F49620-98-1-0313.

Recently, we have observed ultraslow group velocities of light in a solid. Light speeds as slow as 45 m/s were observed, corresponding to a group delay of 66 μs in a 3-mm thick crystal. Reduction of the group velocity is accomplished by using a sharp spectral feature in absorption and dispersion, produced by a Raman excited spin coherence in an optically dense Pr doped Y_2SiO_5 crystal.

Since the first observation of ultraslow light[1], there has been substantial interest in its potential applications. For example, it was proposed that slowing the group velocity of a laser pulse down to the speed of sound in a material can produce strong coupling between acoustic waves and the electromagnetic field[2]. The resultant giant nonlinearity obtained by this method might be utilized for efficient multi-wave mixing and quantum nondemolition measurements[3], as well as for novel acousto-optical devices. A carefully controlled, slow group velocity of light might even allow a very efficient nonlinear interaction between laser pulses of extremely low (down to a single photon) energy[4]. These effects can be used to create quantum entanglement between single photons without an ultrahigh finesse cavity and therefore are of great interest for quantum information processing. Slow light is also of interest because it serves as a useful metric to compare the relative merits of dissimilar nonlinear optical interactions. This is especially important for applications that make use of large optical dispersive properties of EIT[5-9] for the detection of small phase shifts, such as in very sensitive magnetometers.[10]

Initially, ultraslow light was observed in an ultra cold atomic vapor using the sharp dispersion caused by electromagnetically induced transparency (EIT)[11]. EIT, which is related to coherent population trapping[12], uses an intense electromagnetic field is used to modify the absorption coefficient and refractive index seen by a weak probe so that an optically dense media can be made nearly transparent to light at its resonance frequency. In addition, the sharp dispersion of EIT leads to a slow group velocity for the propagation of light, tuned to the frequency of the transparency peak. At first it was believed that only a material with a small inhomogeneous broadening could be used to achieve ultraslow light, but subsequent experiments employing a hot vapors[5,8,13] were soon shown to work better than expected.[5,8] Still, for a number of applications, the need to compensate for Doppler shifts in a hot vapor by using nearly co-propagating laser beams is inconvenient. Finally, for potential technological device applications of ultraslow light, there is no substitute for solids.

Recently, we reported near 100% efficient EIT in a Pr^{3+} doped Y_2SiO_5 (Pr:YSO) crystal[14] wherein transparency of probe field was demonstrated at line center in an optically thick sample. At low temperatures, this "dark resonance" has a width on the order of 10's kHz. This potentially makes it suitable for the direct measurement of ultra long optical group delays because the group delay time for a pulse that propagates one attenuation length is approximately given by to the inverse width of the EIT peak[8] assuming 100% efficient EIT. We would like to note that Pr:YSO and many rare-earth doped crystals have properties similar to both hot and cold atomic vapors. In particular, both Pr:YSO and ultra cold vapors, have the advantage that there is no motional diffusion of atoms, whereas Pr:YSO and hot vapors have the common advantage that the light speed can be slowed to well below the sound speed in the medium.

Our crystal was supplied by Scientific Materials, Inc. and consisted of 0.05 at% Pr doped YSO in which Pr^{3+} substitutes Y^{3+}. The crystal had a thickness of 3 mm in the light propagation direction. To generate the EIT peak, we used the $^3H_4 \rightarrow {}^1D_2$ optical transition with a central frequency of 605.7 nm. The relevant energy level diagram is presented in Figure 1. Here, the coupling and the probe fields, with frequencies ω_C and ω_P respectively, create a coherence the between ground states $^3H_4$ ($\pm 3/2 \leftrightarrow \pm 5/2$), while the repump field with frequency ω_R partially refills the spectral holes burned by the coupling and the probe fields. This partial refilling or anti-hole also provides a narrow effective optical inhomoheneous linewidth for the Raman transitions. The experimental arrangement is similar to that used in Ref. 14. This time, we used a COHERENT 899-21 single mode ring dye laser pumped by an INNOVA 300C argon laser. The dye laser was continuos wave with a laser jitter measured to be about 0.5 MHz. All the laser fields shown in Figure 1 were derived from the dye laser output using acousto-optic frequency shifters. This greatly relaxes dye laser frequency stability requirements since the resonant Raman interaction is insensitive to correlated laser jitter. To match Figure 1, the coupling, repump, and probe beams were downshifted from the original laser frequency by 288.3, 311.0, and 298.5 MHz respectively. To generate the probe beam absorption spectra, the probe frequency was scanned around the 10.2 MHz Raman transition frequency while the frequencies of the coupling and the repump beams were held fixed. A set of compensating galvos was used to correct for the optical alignment changes that arise when the acousto-optic modulators are tuned. The intersection angle of the coupling and probe beams at the crystal was about 4^o in the plane of the optical table. The intersection angle of the repump beam was also 4^o but out of the plane of the optical table. This geometrical arrangement allowed us to reduce the effects of scattered light from the coupling and the repump beams. To further increase the signal to noise ratio, the probe beam was modulated and the transmitted signal was detected by standard phase-sensitive detection techniques. All laser beams were linearly polarized and focused into the crystal by a 150 mm focal length lens, producing a spot with a diameter of about 100 m. The beams were polarized in a common direction that could be rotated by a half-wave plate to maximize absorption for a given orientation of the crystal. During the experiment, the sample was maintained at a temperature of 5.5 K inside a helium flow JANIS cryostat.

The dye laser was locked near the center of the inhomogeneously broadened absorption line at 605.7 nm. The intensities of the probe and repump fields were held fixed during the experiment at 0.1 and 1.6 W/cm^2, respectively. The background absorption was determined by the anti-hole, which was created by the repump beam, and superimposed on the much broader, saturated hole burned by the pump beam. The width of anti-hole was found to be about 0.5 MHz and was defined by the dye laser frequency jitter. The width of the saturated hole was not determined due to the limited 50 MHz bandwidth of the acousto-optic modulators, but appeared to be much larger than 50 MHz. Due to the limited intensity of the coupling field, the maximal transparency was found to be about 50%. Figure 2a shows a representative absorption spectrum of the probe field obtained at a coupling field intensity of 105 W/cm^2. The spectrum was recorded using phase in-sensitive lock-in detection. The measured FWHM of EIT peak was around 60 kHz for the chosen range of coupling field intensities. This is much smaller than the laser jitter of 0.5 MHz and is in agreement with the inhomogeneous linewidth of the spin transition as measured by optically detected nuclear magnetic resonance (ODNMR). The peak absorption of the probe near the

center of the anti-hole line was about 90% and could be adjusted by changing the intensities of the coupling and the repump fields. Blocking either the coupling beam or the repump beam resulted in nearly 100% transparency of the probe beam because of spectral hole burning.

The temporal retardation of the amplitude modulated probe beam tuned to the EIT peak manifests itself as a strong shift in the modulation phase that can be measured with a lock-in amplifier. Figure 2b and 2c show the absorption spectra of the probe beam for two different lock-in amplifier phases. Both spectra were recorded at a coupling beam intensity of 105 W/cm^2 and a probe beam amplitude modulation frequency of 6 kHz. Figure 2b shows the absorption spectrum recorded with the lock-in amplifier phase adjusted to suppress the broad absorption, and Figure 2c demonstrates the same absorption spectrum with the lock-in amplifier phase adjusted to suppress the EIT peak. Comparison of these two spectra clearly shows a strong dependence of the phase of modulation of the transmitted signal on the detuning from the EIT peak. To measure the group delay, the probe field was modulated with a square wave at a frequency that was varied in the range of 3 – 6 kHz. These low modulation frequencies assure that pulse spectrum is contained within the EIT peak. The group time delay was calculated based on the modulation frequency and the phase shift between the transmitted probe signal with and without the EIT-producing coupling field. Figure 3 presents the measured phase shift as a function of modulation frequency for the coupling beam intensity of 105 W/cm^2. The group delay time for this coupling beam intensity was found to be 39.6 μs from the linear fit of the data. This result is in good agreement with an estimate based on the equations in ref. 13 using the measured 62 kHz FWHM of the EIT resonance.

At low coupling beam intensities, the fraction of Pr ions that are pumped into the "dark state" increases with coupling laser power and therefore the depth of the transparency increases. This causes the group delay to increase. At higher intensities, the transparency begins to power broaden, reducing the sharpness of the dispersive feature. This reduces the observed group delay[5]. To show these saturation effects, the EIT peak width and amplitude were measured as a function of the coupling beam intensity and the results are shown in Figure 4. At intensities below 50 W/cm^2 the width of the EIT peak is defined by the inhomogeneous width of the ground state transition, and therefore it is a constant. Meanwhile the amplitude of the EIT peak increases linearly with the intensity. At high intensities above 65 W/cm^2 the width of the peak begins to increase with intensity due to power broadening, while the amplitude of the peak saturates. Comparing this data to Figure 5, which shows the group velocity and delay versus coupling beam intensity, it is apparent that there is a strong correlation between the EIT linewidths and amplitudes and the observed group velocities.

As can be seen in Figure 5, a group velocity of light as slow as 45 m/s is reached. Here, we assumed the length of an interaction zone to be 3 mm, which is the thickness of the crystal. However, due to the geometric configuration used, the interaction area where all three beams are overlapping is slightly shorter than the thickness of the crystal, so that the actual group velocities are slightly smaller than in Figure 5. In contrast to the slow light experiment in an optically dense hot vapor[13], the light velocity here is practically independent of the propagation distance since the intense coupling beam propagates with little attenuation. However, as shown in Figure 5 the dependence of the group velocity on the input coupling field intensity still permits fine tuning of the group delay so as to allow one to achieve phase-matched conditions in an experiment on stimulated Brillouin scattering[2] and/or to adjust group velocities of single photons for ultrastrong nonlinear interaction[4].

To summarize, we have demonstrated an ultraslow group velocity of light of 45 m/s in a rare-earth doped crystal, which is fundamentally limited only by the inhomogeneous broadening of the ground state transition. This first observation of ultraslow light in a solid is an key enabling step toward many potential applications of slow light to low-intensity nonlinear optics, quantum information processing, as well as to technological

References

1. L. V. Hau, S. E. Harris, Z. Dutton, C. Behroozi, Nature, **397** (1999) 594.
2. A. Matsko, Y. Rostovtsev, H. Cummins, M. Scully, Phys. Rev. Lett. **84** (2000) 5752.
3. V. Braginsky, F. Khalili, Quantum Measurement (Cambridge University Press, 1992).
4. M. Lukin, A. Imamoglu, Phys. Rev. Lett. **84** (2000) 1419.
5. O. Schmidt, R. Wynands, Z. Hussein, D. Meschede, Phys. Rev. A., **53** (1996) R27.
6. M. Xio, Y. Li, S. Jin, J. Gea-Banacloche, Phys. Rev. Lett., **74** (1995) 666.
7. S. E. Harris, L. V. Hau, Phys. Rev. Lett., **82** (1999) 4611.
8. S. E. Harris, J. E. Field, A. Kasapi, Phys. Rev. A, **46** (1992) R29.
9. A. Kasapi, M. Jain, G. Y. Yin, S. E. Harris, Phys. Rev. Lett., **74** (1995) 2447.
10. M. O. Scully, M. Fleischhauer, Phys. Rev. Lett., **69** (1992) 1360.
11. S. E. Harris, Physics Today, July 1997, 36.
12. E. Arimondo, in Progress in Optics, Edited by. E. Wolf (Elsevier Science, Amsterdam, 1996) p. 257.
13. M. Kash, V. Sautenkov, A. Zibrov, L. Hollberg, G. Welch, M. Lukin, Y. Rostovsev, E. Fry, M. Scully, Phys. Rev. Lett., **82** (1999) 5229.
14. B. Ham, P. Hemmer, M. Shahriar, Optics Commun. **144** (1997) 227.

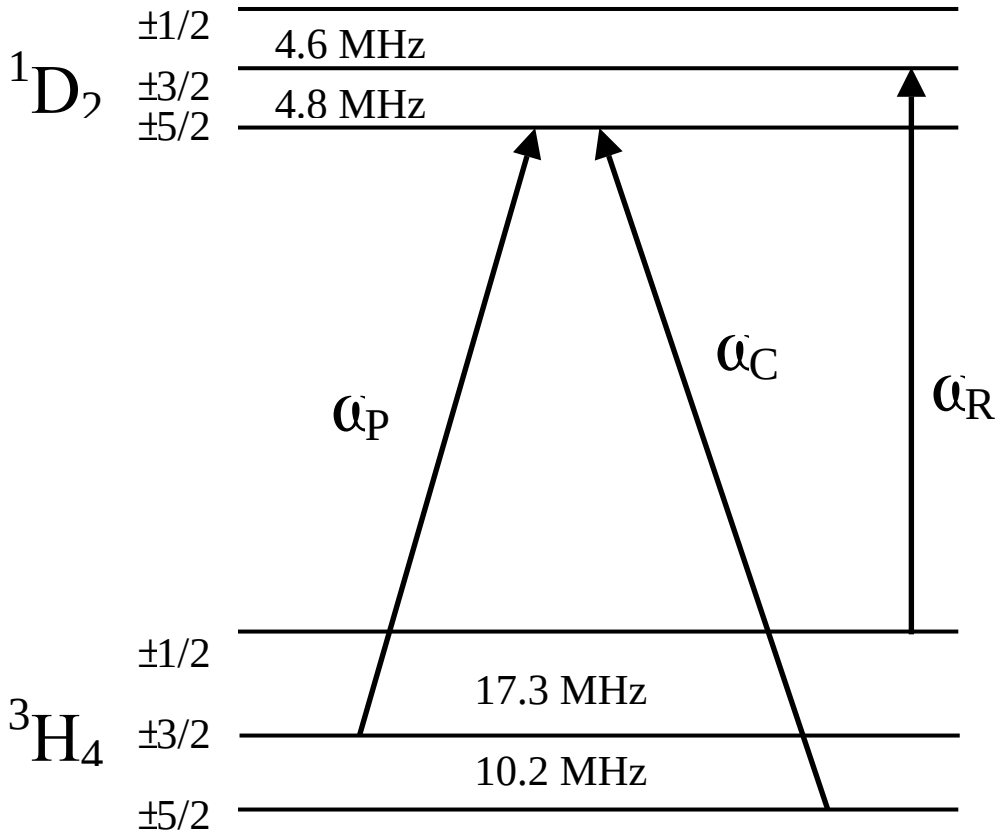

Figure 1. Energy level diagram of Pr:YSO. ω_C, ω_R, and ω_P are frequencies of the coupling, the repump, and the probe fields, respectively.

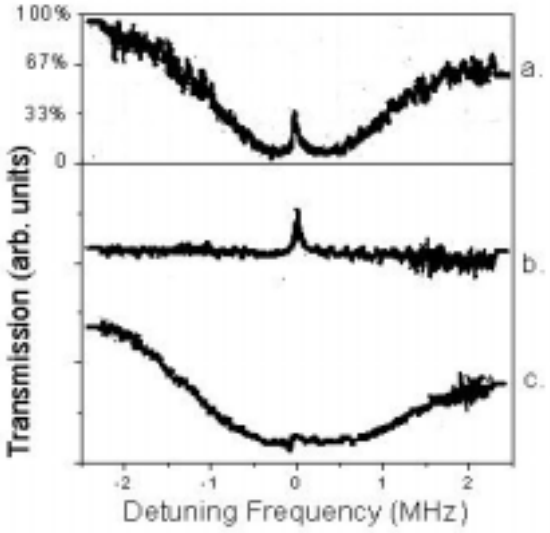

Figure 2. The absorption spectra of the probe beam at 5.5 K for a coupling field intensity of 105 W/cm^2. (a) spectrum recorded by phase in-sensitive lock-in detection; (b) spectrum recorded by phase sensitive lock-in detection with the phase adjusted to suppress the anti-hole absorption; (c) the spectrum (b) recorded with the phase adjusted to suppress the EIT peak. The modulation frequency of the probe beam was 6 kHz in for all three traces.

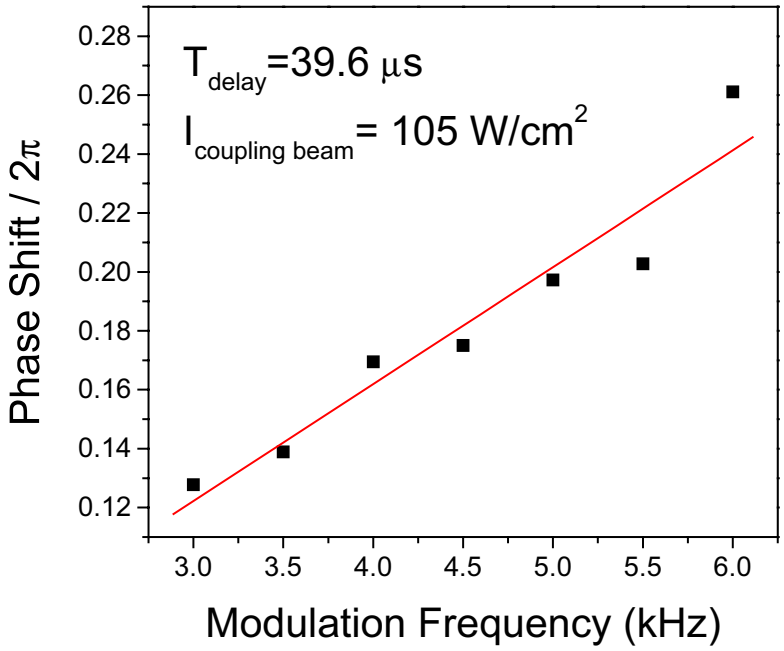

Figure 3. Phase shift between the transmitted probe signal with and without the coupling field vs. modulation frequency. The delay time was found to be 39.6 μs from the linear fit of the data.

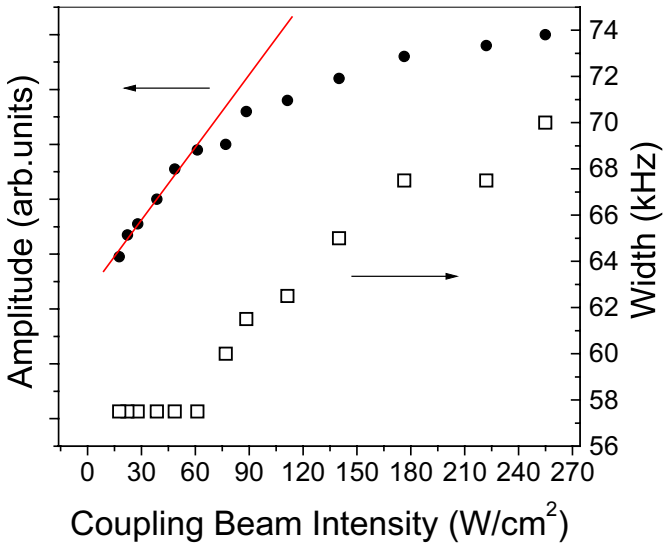

Figure 4. The EIT peak amplitude (closed squares) and width (open circles) vs. coupling beam intensity.

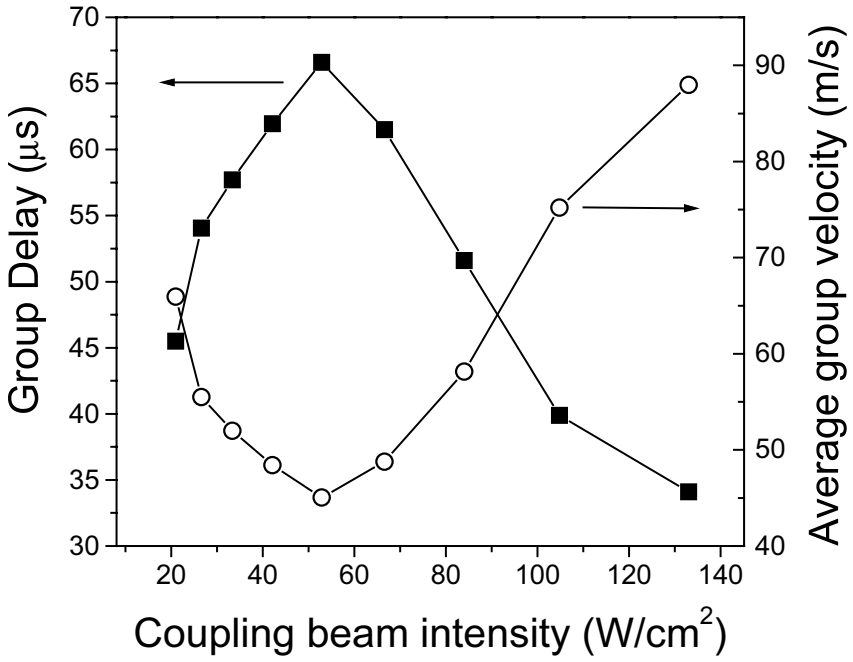

Figure 5. Measured group delays (solid squares) and deduced group velocity (open circles) vs. the intensity of the coupling field.

2. Progress Towards Quantum Computing Using NV Diamond

Sponsors
AFOSR grant #F49620-98-1-0313, ARO grant # DAAG55-98-1-0375

Previously, we reported on our design for a quantum computer via spectral hole-burning, followed by observation of optically induced spin alignment in NV-Diamond as a first step towards realizing such a computer. Here, we report further advances in the experimental work. In addition, we report on the design of a photonic band-gap based cavity in NV-Diamond for coupling quantum bits efficiently, and on our efforts towards detecting individual NV color centers. These two steps are critical for realizing an array of distinct quantum bits coupled to its nearest spectral neighbor. Finally, we discuss how this approach may lead to a large scale, type-II quantum computer.

A quantum computer (QC) that stores information on two-state systems called quantum bits or qubits must be able to address and manipulate individual qubits, to effect coherent interactions between pairs of qubits, and to read out the value of qubits.[1,2] Current methods for addressing qubits are divided up into spatial methods, as when a laser beam is focused on an individual qubit[3,4,5] or spectral methods, as when a nuclear spin in a molecule is addressed using NMR.[6,7] The density of qubits addressable spatially is limited by the wavelength of light, and the number of qubits addressable spectrally is limited by spin linewidths. Previously, we reported a method for addressing qubits using a technique that combines spatial and spectral selectivity. The result is a design for quantum computation that provides the potential for a density of quantum information storage and processing many orders of magnitude greater than that afforded by ion traps or NMR. Specifically, this method uses an ensemble of spectrally resolved atoms in a spectral holeburning solid such as NV-diamond.

The basic concept is recalled briefly in figure 1. Consider a small volume element of a crystal containing a set of impurity atoms. Each atom sees a unique surrounding, so that the resonance frequency for a given transition is different for different atoms. The number of spectrally resolvable bands, N_R, is determined by the ratio of the spectral spread to the width of the individual resonance. We consider a situation where the number of atoms in the selected volume is less than N_R, so that each atom can be addressed individually. For the basic model, we can consider each atom to have two metastable states, representing the spin up and down, for example, coupled to an excited state via optical frequency transitions; this is often called a Λ transition. The energy splitting (ε) between the metastable states establishes the frequency spacing between the sets of atoms that can be coupled to one another via nearest neighbor interactions. Note that in this model two atoms (M and M+1, in figure 1b, for example) are considered to be spectrally adjacent when the lower frequency optical transition of one (e.g. atom M) is degenerate with the higher frequency optical transition of the other (atom M+1). Here, each quantum bit (qubit) can be viewed as a composite spin, and the coupling between spectrally adjacent qubits is mediated by optical dipole-dipole interactions, which can be enhanced by enclosing the qubits in a high finesse optical cavity that is resonant at the frequency common to both atoms. The number of coupled qubits that can be realized this way is given by the ratio of the inhomogeneous width to the energy spacing ε. This number can in principle be as high as 10^5 in NV-diamond.

In this model, an individual QC is realized in the small volume element. If photonic band gap (PBG) based cavities are used (as discussed later) for coupling the qubits in each of these volume elements, one can realize many (more than 10^4) independent QC's running in parallel. This approach is ideally suited for what is known as *type II quantum computing* (TTQC). Briefly, TTQC is an architecture where many QC's are used simultaneously to perform tasks such as studying lattice gas dynamics, which is turn is useful for simulating complex phenomena such as turbulent flows[19]. Differing from a globally phase-coherent QC, a TTQC requires only local entanglement of the qubits in each constituent QC per node to achieve exponential speedup in

simulations. This architecture is much easier to implement with current technology and will result in the short-term realization of a quantum computer that out-performs the present-day classical supercomputers on certain important problems of DoD interest. Creating a scalable TTQC is also a first enabling step towards building a quantum computer that can run Grover's or even Shor's algorithms. For the NV-diamond based architecture, the combination of a high number of qubits in each QC (300), the large number of operations that can be performed before decoherence (10^3), and the fact that many such QC can be realized on single chip (10^4), is likely to result in a TTQC with unprecedented computing abilities.

One of the most important criteria in making a quantum computer is that one must be able to realize a CNOT operation between two nearest-neighbor qubits. We have identified in explicit detail two different methods for achieving this objective in NV-diamond. The first method[24], applicable to high-density of color centers, uses the direct optical dipole-dipole coupling between two qubits (via the shared blue transition in figure 1b) that are very close to each other spatially, and can be turned into spectral neighbors via applying a magnetic field. This method is somewhat limited in the number of bits that can be coupled. The second method[22], applicable to low-density of color centers, uses a high-finesse optical cavity, resonant with a transition common to both bits (blue transition in figure 1b), to enhance the optical dipole-dipole coupling. As mentioned above, the number of qubits that can be realized this way can in principle be as high as 10^5. While such a high number would be difficult to realize in practice, it should be possible to realize a more modest number (~300) qubits without much trouble.

For efficient cavity-induced coupling, a high value of Q ($2X10^5$) is achievable using the so-called super-mirrors, manufactured by the Research Electro Optics, Inc., of Boulder, CO. However, this number is virtually impossible to achieve in the presence of NV-diamond between the cavity mirrors. Even a small amount of loss resulting, for example, from Fresnel reflections will reduce the Q by orders of magnitude. As such, the idea of using bulk super mirrors of this type is essentially impracticable.

In principle, one could overcome this problem by making the cavity volume small enough so that the ratio of the vacuum rabi-frequency to the cavity decay rate becomes favorable. However, in order to allow unimpeded access of the control-lasers, the separation between the mirror surfaces has to be at least 5 to 10 times the wavelength of interest (λ~637 nm). Furthermore, the machining process used to taper the tips of the mirrors constraints the lateral dimensions to at least a 100 μm. Under these constraints, it is virtually impossible to make the vacuum rabi frequency stronger than the anticipated poor cavity decay rate in the presence of reflection losses from the surfaces of the embedded crystal. A photonic band gap (PBG) cavity holds the best promise to overcome this constraint. The small mode volume of the PBG cavities (on the order of λ^3) implies that the coupling of cavity photons to atoms in the cavity will be enhanced by three or more orders of magnitude over conventional bulk-mirror based cavity couplings. As a result, the number of operations that can be performed before decoherence will be higher by nearly the same ratio.

Another key feature of this approach is that a large number of PBG cavities can be realized on the same substrate. Intercoupled qubits inside each cavity will constitute a single QC. As such, the whole substrate will contain many QC's that can be operated simultaneously. As mentioned above, such a structure is ideally suited for TTQC on a large scale.

We have developed a concrete design to realize a PBG cavity in NV-Diamond in order to demonstrate the feasibility of a QC array where (i) each QC will have a large number of coupled qubits, (ii) the total number of QC's can be very high, as suited for type II quantum computing, and (iii) many operations can be performed before decoherence. We will use a variation of the method demonstrated recently by Masuda et al.[28] to realize the PBG structure necessary for quantum computing. First, a custom-mask will be made using lithographic techniques. The pattern on the mask will then be transferred to an NV-diamond crystal surface using chemical

etching. The resulting structure will consist of a two dimensional periodic array of holes, with periodicity of the order of the wavelength (λ~637 nm) of interest. The symmetry will be broken by replacing a 3X3 grid of these holes with a hole of a larger diameter. The area around this anomalous hole will constitute the cavity, with a mode volume of the order of a few λ^3. Many such cavities will be formed on the same substrate. An important element of our quantum computing protocol requires that the cavity resonance frequency be tunable rapidly, in order to move the coupling process from one set of spectral neighbors to a different one. In order to achieve this capability, the anomalous hole in the center of the cavity will be filled with a non-linear glass. The cavity frequency then can be tuned simply by applying a suitably intense laser beam, which can be done very rapidly.

We have already observed experimentally some of the key features necessary for realizing a quantum computer using NV-diamond. The results are described in detail in ref. 23. Briefly, an NV-diamond crystal, embedded in a cryostat operating at around 4K,is addressed by multi-frequency laser beams generated from an Argon-pumped dye laser at around 637 nm (fig. 2). A magnetic field of about 1 kGauss is applied, so that the relevant energy levels correspond to the desired non-degenerate structure. A simplified view of the energy levels and laser frequencies are shown on the left half of fig. 3a.

Figure 3a also shows the evidence of a spatially (on optical wavelength scale) varying spin-orientation grating, observed via diffraction of a laser beam. The grating is produced by two other frequencies that cause two-photon mediated spin alignments. By controlling the phase difference between these two beams, one can produce any desired state for a collection of color-center spins at a given location. As such, this demonstrates single qubit operations, albeit on a collection of qubits. Before demonstrating these operations on individual qubits, we must develop the set-up for (i) preparing single color centers in an individual channel, and (ii) observing signals from a single qubit, as described above.

Figure 3b shows the evidence of highly efficient preparation of all the spins in a pure state, observed in the form of electromagnetically induced transparency. The observed degree of purity is less than 100% only because of our inability to saturate the inhomogeneously broadened transitions due to the limitation of laser powers, constrained in turn by the efficiencies of the AOMs used. Theoretical estimates carried out by us[23] supports this claim.

We have determined in detail that NV-diamond has the requisite energy levels as well as favorable lifetimes for realizing a multibit quantum computer. Several theoretical constructs have been developed (as discussed above, and described in refs. 22, 24, and 27) to address specifically the approach that is necessary for producing coupled qubits in this medium. Finally, preliminary experiment described above demonstrates clearly that this medium is ready for proceeding to the next step where we will concentrate on demonstrating entanglement between multiple qubits, and demonstrate the feasibility of a type II QC using NV-diamond.

The basic design we have developed for realizing PBG cavities in diamond is illustrated in figure 4. Up to 10^4 cavities will be formed on the same substrate, as illustrated in figure 6. The structure shown in figure 4 consists essentially of a thin film of diamond, sandwitched between two glass surfaces of lower index for the vertical confinement of the cavity mode. The PBG configuration is produced by the presence of a periodic array of holes of the same diameter, with a larger diameter hole replacing a 3X3 grid of this pattern. The anticipated mode pattern is illustrated schematically by the red circle. The color centers under the red circle will be the qubits, coupling to one another through the cavity photons.

The first step will be to perform finite-element type simulations of Maxwell's equations in order to optimize the parameters of this design[29]: the thickness of the diamond layer, the diameter of the periodic holes, and the diameter of the anomalous hole. The primary criterion optimization is to

maximize the Q of the cavity. One has to also calculate the exact mode pattern, and determine the value of the vacuum rabi frequency.

Figure 5 illustrates schematically the multistage layering and etching process to be used to realize the PBG cavity array in NV-diamond. These steps can be implemented using the facilities of the Materials Technologies Laboratory at MIT. The starting point is a thick SiO_2 wafer, with an area close to 1 cm^2, available commercially. Microwave enhanced chemical vapor deposition (CVD) will be used to deposit a synthetic diamond film on this substrate. Nitrogen vacancy color centers will then be created using ion implantation, followed by annealing at 750 C. This will be followed by the growth of five additional thin layers on the diamond film: SiO_2, alumina, polyimide, SiO_2, and PMMA, as shown here.

The desired pattern of holes may be generated using a CAD program. This pattern will then be transferred to the PMMA substrate using E-beam lithography. A series of etching steps, with different ions (as shown on the right of the diagram in figure 5) will be used to transfer this pattern to the diamond. The choice of reactive ions is dictated by the need to avoid etching of the masks. For example, alumina is resistant to the oxygen plasma used for etching the holes in diamond. Finally, the holes in diamond will be filled with a non-linear optic material. Excess material above the top SiO_2 layer will be removed chemically, leaving the structure shown in fig. 4.

Once we develop the PBG cavities in NV-diamond, we will be in a position to realize the scheme of coupling two qubits via a cavity photon, in order to demonstrate a CNOT gate. In order to achieve this goal, we will first determine the transition frequency, the vacuum rabi frequency, and the Q of one of the cavities. This will be done as follows. A single color center at the cavity location will be optically pumped into one of its hyperfine states. A laser π-pulse will be applied along one of the legs of the Λ transition (red transition in fig. 1b, for example). The population in the other hyperfine state will then be measured by applying a laser along the other leg (blue transition in fig. 1b) of the Λ transition. This process will be repeated many times while the cavity is tuned by varying the intensity of the auxiliary laser beam applied to modulate the index of the non-linear glass in the holes. The signal observed will be maximum when the cavity is tuned to the second leg (blue transition in fig. 1b) of the Λ transition. The amplitude of this resonant peak can be used to determine the strength of the cavity field, i.e., the vacuum rabi-frequency. The width of the resonance will reveal the Q of the cavity. Once the cavity is characterized, we will identify and isolate two color centers that are spectral neighbors (e.g., M and M+1 in fig. 1b). The steps described in previous reports for demonstrating a CNOT gate will then be implemented.

As mentioned above, one of the conditions for realizing a CNOT gate is the ability to isolate and detect single color centers. Techniques for spectral isolation via shelving has been described in detail in ref. 22. We have made recent experimental progress towards spatial isolation and detection. Briefly, we used a diamond sample with color centers on its surface. Figure 7 shows the basic geometry used. Two acousto-optic modulators were used to scan a laser beam in two dimensions, while remaining focused on the surface of the sample. The fluorescence generated was collected with a microscope objective, filtered, and then detected using a Geiger mode avalanche photo diode (APD). The scanning process was controlled by a DAC card installed in a computer, which also recorded the two dimensional image resulting from the raster scan. A typical scan obtained this way is shown in figure 8. The deep purple line shows one of the lines of color centers. An isolated cluster of color centers is seen about 10 μm away. The next step is to use the optical shelving technique described in ref. 22 to reduce the active number of centers to unity in such a cluster.

References:

1. S. Lloyd, “A Potentially Realizable Quantum Computer,” *Science*, Vol. **261**, pp. 1569-1571 (1993).

2. D.P. DiVincenzo, "Quantum Computation," *Science*, Vol. **270**, pp. 255-261 (1995).
3. J.I. Cirac and P. Zoller, "Quantum Computations with Cold Trapped Ions," *Physical Review Letters*, Vol. **74**, pp. 4091-4094 (1995).
4. T. Pellizzari, S.A. Gardiner, J.I. Cirac, P. Zoller, "Decoherence, Continuous Observation, and Quantum Computing: a Cavity QED Model," *Physical Review Letters*, Vol. **75**, pp. 3788-3791 (1995).
5. C. Monroe, D.M. Meekhof, B.E. King, W.M. Itano, D.J. Wineland, "Demonstration of a Fundamental Quantum Logic Gate," *Physical Review Letters*, Vol. **75**, pp. 4714-4717 (1995)
6. D.G. Cory, A.F. Fahmy, T.F. Havel, "Nuclear Magnetic Resonance Spectroscopy: an experimentally accessible paradigm for quantum computing," in *PhysComp96*, Proceedings of the Fourth Workshop on Physics and Computation, T. Toffoli, M. Biafore, J. Leao, eds., New England Complex Systems Institute, 1996, pp. 87-91.
7. N.A. Gershenfeld and I.L. Chuang, "Bulk Spin-Resonance Quantum Computation," *Science*, Vol. **275**, pp. 350-356 (1997).
8. A. Barenco et al., "Elementary Gates for Quantum Computation," *Phys. Rev. A.,* Vol. **52**, pp. 3457-3467 (1995).
9. S. Lloyd, "Almost Any Quantum Logic Gate is Universal," *Physical Review Letters*, Vol. **75**, pp. 346-349 (1995).
10. R.M Macfarlane and R.M. Shelby, "Coherent transient and holeburning spectroscopy of rare earth ions in solids," in *Spectroscopy of solids containing rare earth ions*, A.A. Kaplyanskii and R.M MacFarlane, eds. (Elsevier Science Publishers B.V., 1987) pp. 51-184.
11. H. Lin, T. Wang, and T. W. Mossberg, "Demonstration of 8-Gbit/in^2 areal storage density based on swept-carrier frequency-selective optical memory," *Optics Letters*, Vol. **20**, 1658-60 (1995); X. A. Shen, E. Chiang, and R. Kachru, "Time-domain holographic image storage," *Optics Letters* **19**, 1246-1248 (1994)
12. E. VanOort, M. Glasbeek, "Optically detected low field electron spin echo envelope modulations of fluorescent N-V centers in diamond," *Chemical Physics*, Vol. **143**, 131 (1990); X.F. He, N.B. Manson, P.T.H. Fisk, "Paramagnetic resonance of photoexcited N-V defects in diamond. I. Level anticrossing in the ^{3}A ground state," *Physical Review B* **47**, 8809 (1993).
13. L. Viola and S. Lloyd, "Dynamical suppression of decoherence in two-state quantum systems," *Physical Review A,* Vol. **58**, 2733-43 (1998).
14. R.W. Equall, R.L. Cone, and R.M. Macfarlane, "Homogeneous broadening and hyperfine structure of optical transitions in Pr^{3+}:Y_2SiO_5," *Physical Review B*, Vol. **52**, 3963-69 (1995), and references therein.
15. D.J. Heinzen, J.J. Childs, J.E. Thomas, M.S. Feld, "Enhanced and inhibited visible spontaneous emission by atoms in a confocal resonator," *Physical Review Letters,* Vol. **58**, 1320-3 (1987).
16. S.E. Morin, C.C. Yu, T.W. Mossberg, "Strong atom-cavity coupling over large volumes and the observation of subnatural intracavity atomic linewidths," *Physical Review Letters*, Vol. **73**, 1489-92 (1994)
17. C.H. Bennett, D.P. DiVincenzo, J.A. Smolin, "Capacities of quantum erasure channels," *Physical Review Letters*, Vol. **78**, (1997)
18. S.J. van Enk, J.I. Cirac, and P.Zoller, "Purifying two-bit quantum gates and joint measurements in cavity QED" *Physical Review Letters*, Vol. **79**, pp. 5178-81 (1997)
19. J. Yepez, *Intl. J. Mod. Phys.* 9 pg 1587 (1998); J. Yepez, QCQC'98 *Lecture Notes in Comp Sci.* 1509, Springer, pg 34 (1998); see web page http://xyz.plh.af.mil/.
20. D.A. Redman, S.W. Brown, and S.C. Rand, "Origin of persistent hole burning of N-V centers in diamond," J. Opt. Soc. Am. B., **9**, 768 (1992)
21. C. J. Hood, M. S. Chapman, T. W. Lynn, and H. J. Kimble, "Real-time cavity QED with single atoms," *Physical Review Letters*, Vol. **80**, 4157-4160 (1998)
22. M.S. Shahriar, P.R. Hemmer, S. Lloyd, J. Bowers, and A.E. Craig, "Quantum Computing via Spectral Hole Burning," *quant-ph/0007114,* submitted to *Science.*
23. A.Turukhin, J. Musser, P.R. Hemmer, and M.S. Shahriar, "Raman Excited Spin Coherence in Diamond," quant-ph/0007114, to appear in *Optics Letters*.

24. M.D. Lukin and P.R. Hemmer, “Quantum Entanglement via Optical Control of Atom-Atom Interactions,” Phys. Rev. Lett. **84** (2000) 2818.
25. S.Lloyd, M.S. Shahriar, and P.R. Hemmer, *quant-ph/0003147*; also see the cover article by Justin Mullins,*Quantum Internet: Teleporting Round the World*, in New Scientist, May 20, 2000 (p. 26)
26. L. Viola, S. Lloyd, and E. Knill, “Universal Control of Decoupled Quantum Systems,” *Phys. Rev. Letts. 83*, 4888(1999).
27. M.S. Shahriar, “Cavity Induced Coherence Transfer for Production of Entanglement Between Atoms with Non-degenerate metastable states,” , submitted to *Phys. Rev. A.*
28. H. Masuda, M. Watanabe, K. Yasui, D. Tryk, T. Rao, and A. Fujishima, “Fabrication of a Nanostructured Diamond Honecomb Film,” *Adv. In Materials*, vol. 12, p.444 (2000).
29. Joannopoulos, Meade, and Winn, “Photonic Crystals,” Cambridge University Press, 1998.

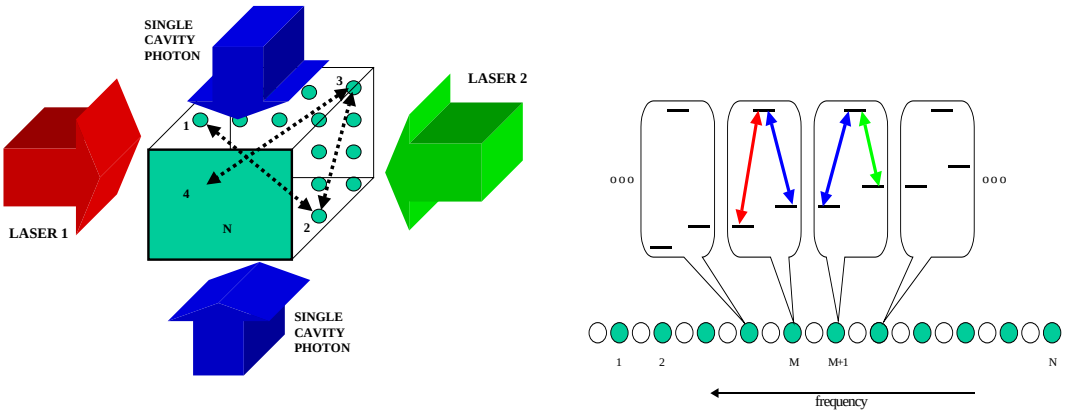

(a) **(b)**

Figure 1: Schematic Illustration of coupling inhomogeneously broadened atoms using spectral selectivity. Figure 1a shows a small volume of a crystal, selected by the intersection of the cavity mode and the control laser beams. Figure 1b shows how the atoms can be indexed in terms of their frequency response. Spectrally adjacent atoms, with a frequency difference matching the ground state splitting, can be coupled selectively by tuning the cavity and the coupling lasers. Atom M can be addressed spectrally via the red transition, atom M+1 can be addressed via the green transition, and the two are coupled to the cavity via the blue transition. The key constraint on the matching is that the Λ transition in each atom must be two-photon resonant. This can be realized by choosing the laser frequencies appropriately. It is also necessary to make sure that there is only one atom per spectral channel.

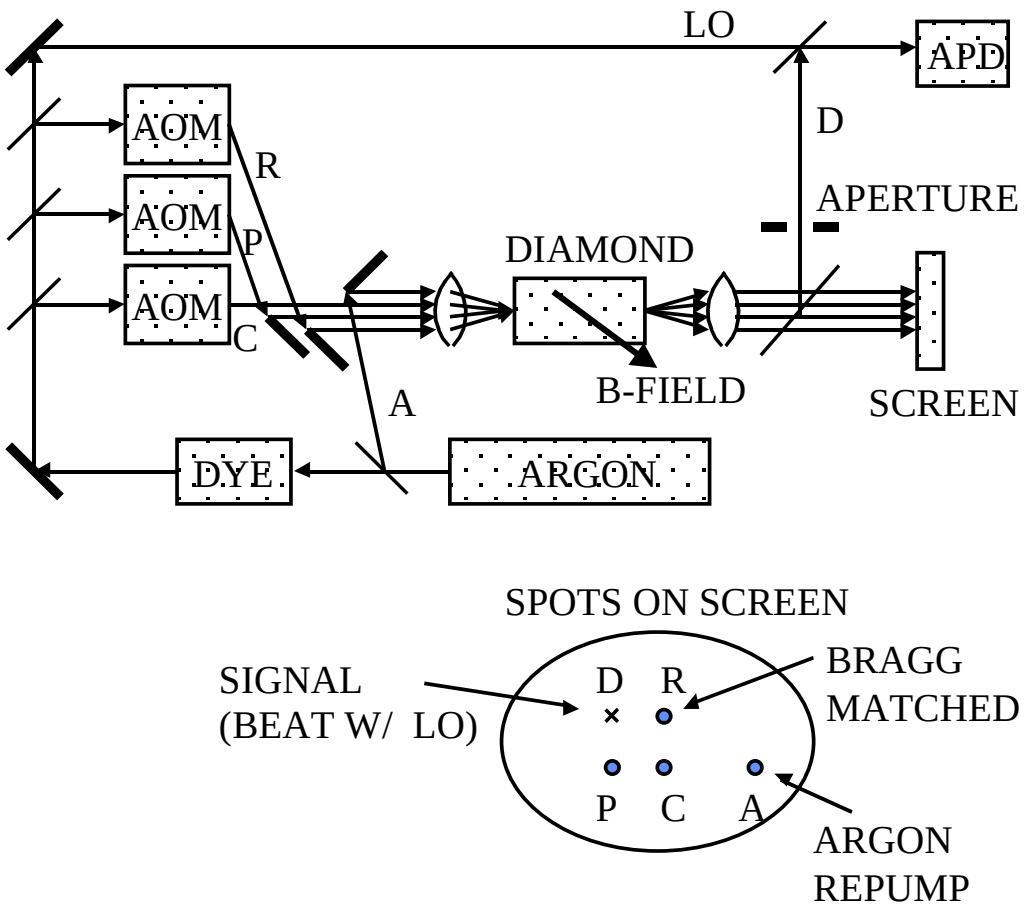

Figure 2: Schematic illustration of the experimental setup used for observing single bit operations on a collection of color centers in NV-diamond. The diamond crystal is housed in a helium cryostat, inside a chamber with anti-reflection coated windows. A water-cooled coil is used to produce a magnetic field close to 1000 Gauss. The coil is mounted on a precise, two dimensional rotation stage for optimal alignment of the magnetic field.

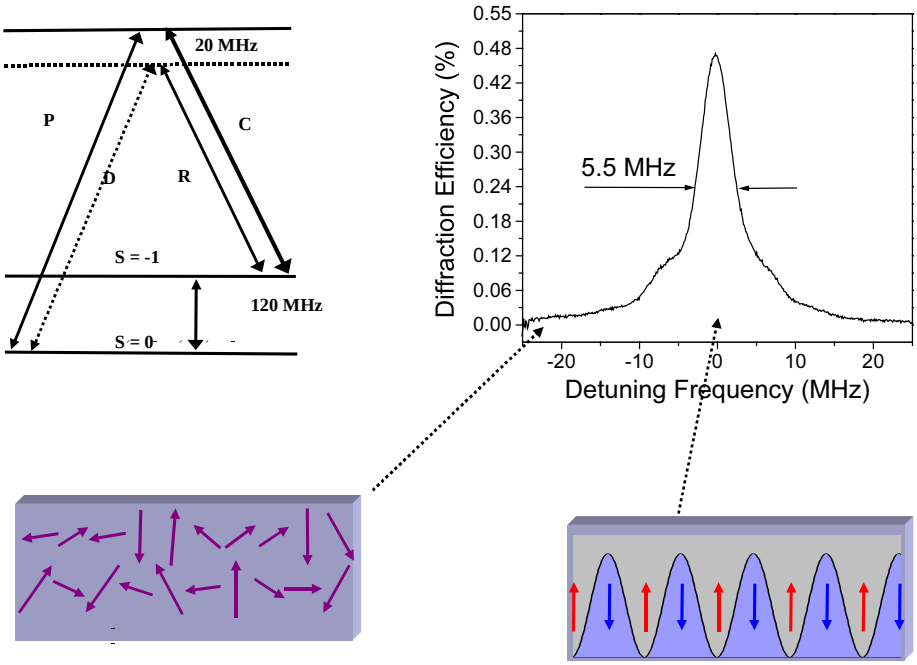

[A]

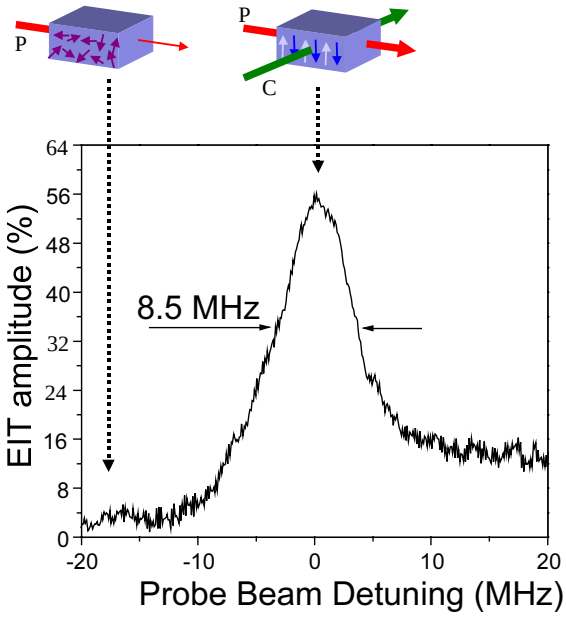

[B]

Figure 3: (a) Demonstration of single bit operations on a collection of color centers, observed via diffraction from a spin grating, (b) High degree of spin orientation (near-perfect for a sub-set of individual color centers, when spin inhomogeneous broadening is taken into account), observed as electro-magnetically induced transparency.

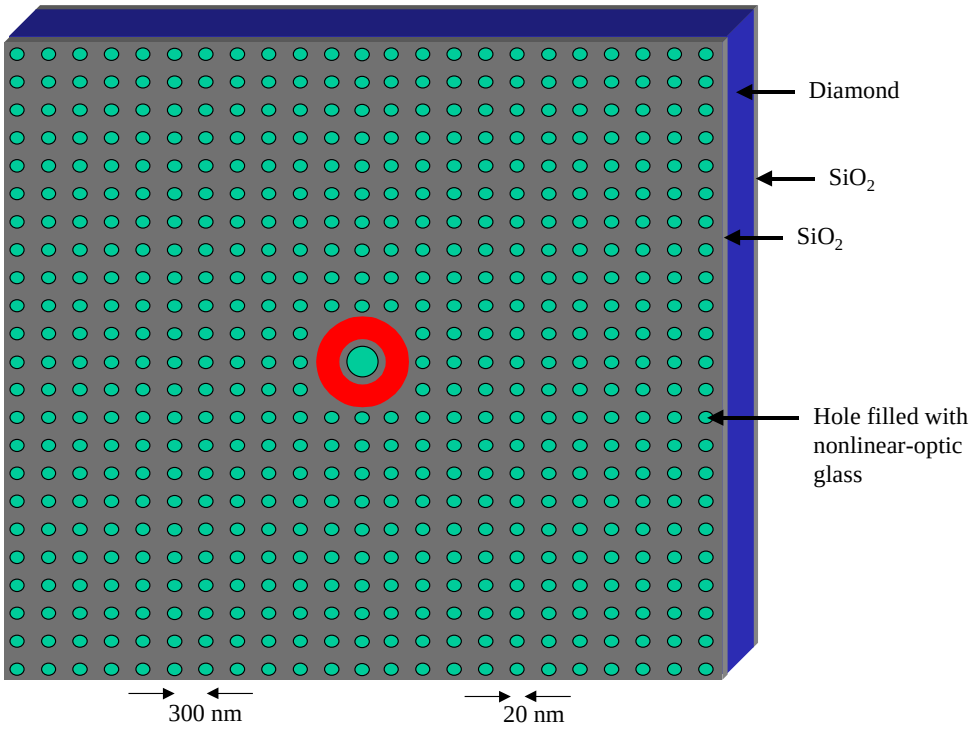

[A]

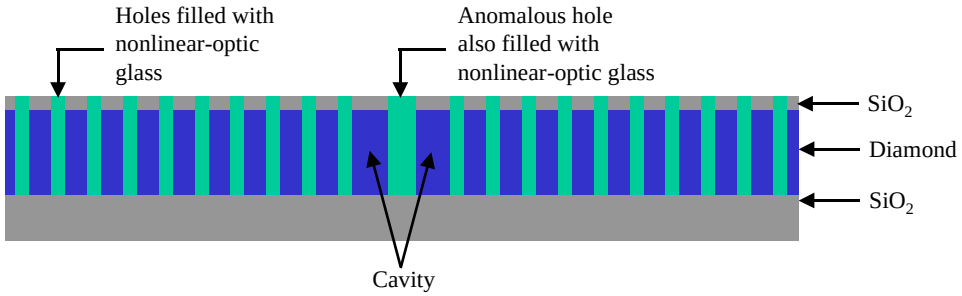

[B]

Figure 4. Schematic illustration of the proposed PBG cavity structure in NV-Diamond. (a) Top view (b) Cross-sectional view. This will be one of many (up to 10^4) cavities formed on the same substrate, as illustrated in figure 9. The pattern shown here can be produced using the multi-stage process summarized in figure 8. The finished structure shown here consists essentially of a thin film of diamond, sandwitched between two glass surfaces of lower index for the vertical confinement of the cavity mode. The PBG configuration is produced by the presence of a periodic array of holes of the same diameter, with a larger diameter hole replacing a 3X3 grid of this pattern. The anticipated mode pattern is illustrated schematically by the red circle; of course, the real pattern will have some asymmetry. The color centers under the red circle will be the qubits, coupling to one another through the cavity photons.

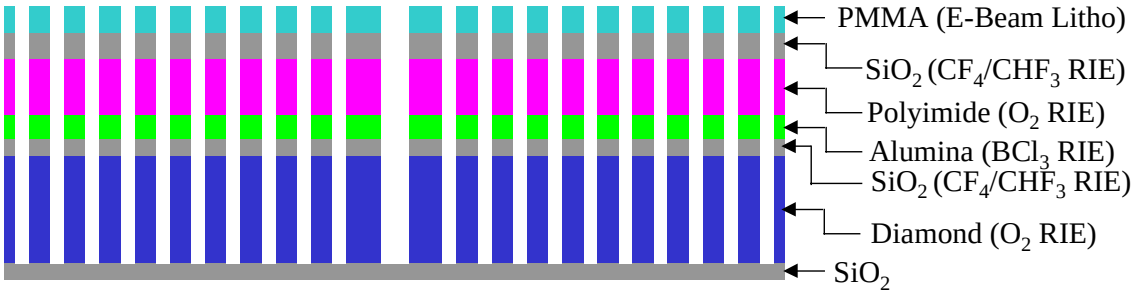

Figure 5. Schematic illustration of the proposed multistage layering and etching process, to be implemented using the facilities of the materials technologies laboratory at MIT. The starting point is a thick SiO_2 wafer, with an area close to 1 cm^2, available commercially. Microwave enhanced chemical vapor deposition (CVD) will be used to deposit a synthetic diamond film on this substrate. Nitrogen vacancy color centers will then be created using ion implantation, followed by annealing at 750 C. This will be followed by the growth of five additional thin layers on the diamond film: SiO_2, alumina, polyimide, SiO_2, and PMMA, as shown here. The desired pattern of holes will be generated using a CAD program. This pattern will then be transferred to the PMMA substrate using E-beam lithography. A series of etching steps, with different ions (as shown on the right of the diagram) will be used to transfer this pattern to the diamond. The resulting holes will then be filled with a non-linear optic material. Excess material above the top SiO_2 layer will be removed chemically, leaving the desired structure.

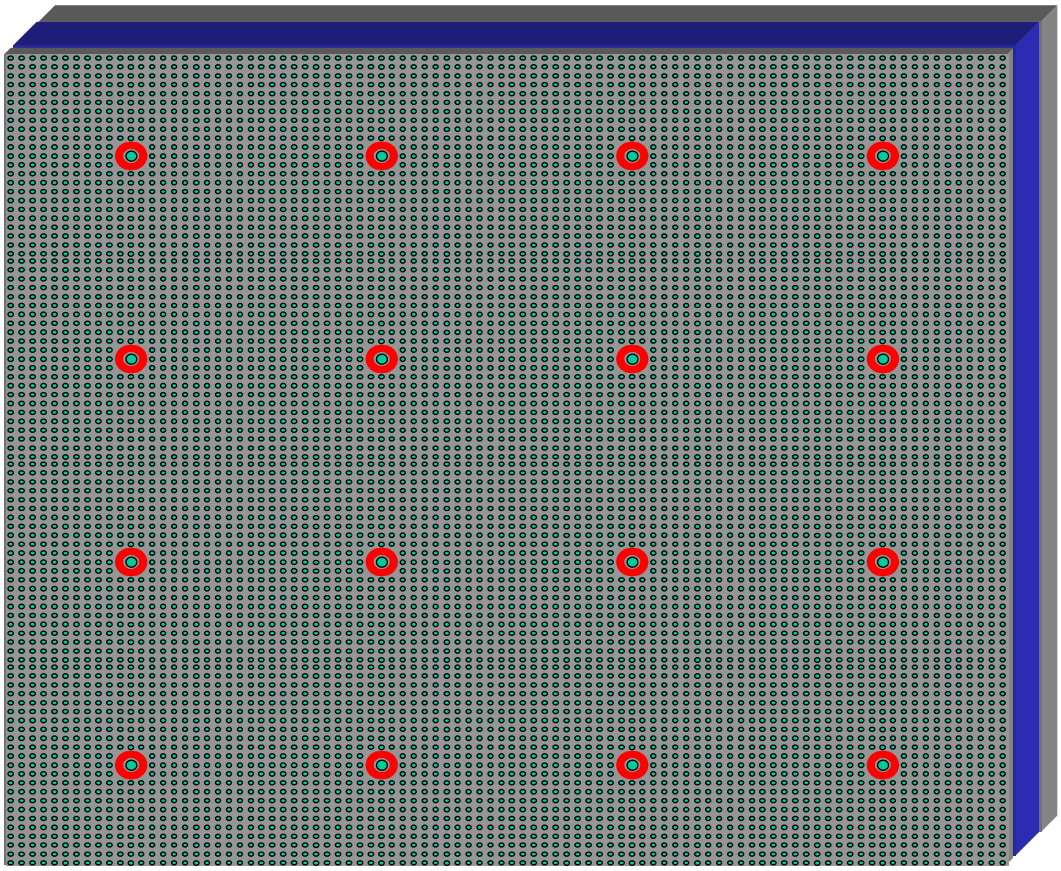

Figure 6: Schematic view of the array of PBG cavities for Type II quantum computing. Here, each cavity represents a single QC. The total number of QC's on a single chip with an area of 1 cm^2 can be easily as high as 10^4. A computer-controlled, analog spatial-light modulator (available in sizes as large as 1000X1000 elements) can be used to control the intensities of the laser beams for each QC separately. Of course, such independent controls are necessary only for general purpose quantum computing. For type II quantum computing, on the other hand, all the QC's can in principle be operated in an identical manner, thereby simplifying the programming task enormously.

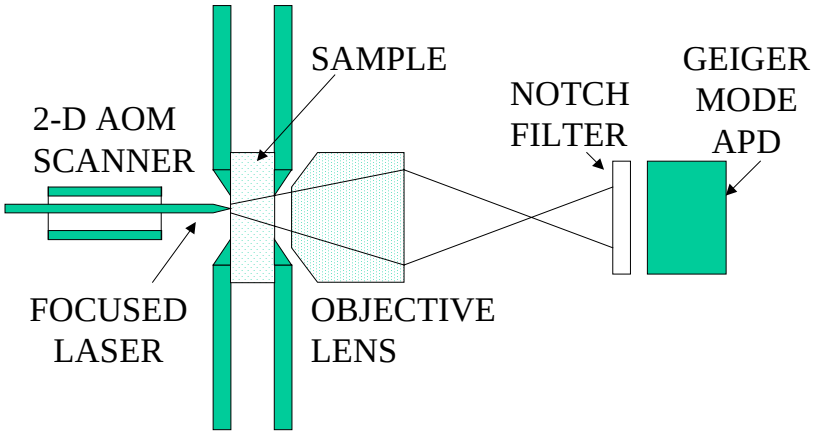

Figure 7. Schematic illustration of the configuration used for detecting small clusters of color centers on the surface of a diamond crystal. When combined with spectral shelving described in ref. 22, this technique will enable the detection of single color centers.

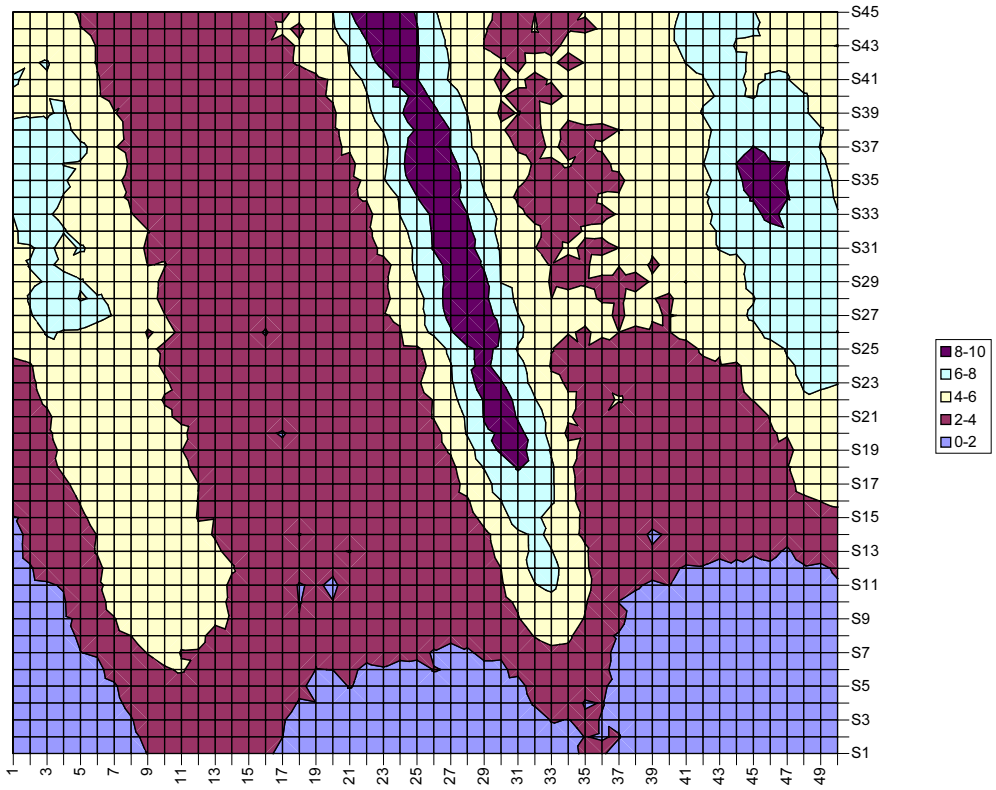

Figure 8. A typical raster scan of the surface of a diamond crystal with color centers created on its surface, using the apparatus of figure 7. The deep purple line shows one of the lines of color centers. An isolated cluster of color centers is seen about 10 μm away. The next step is to use the optical shelving technique described in ref. 22 to reduce the active number of centers to unity in such a cluster.

3. Progress Towards Realization of a Large Area Atom Interferometer for Nanolithography: Observation of Robust Atom Interferometry Using a Single-Zone Optical Field

Sponsor
AFRL contract #F19628-00-C-0074

Previously, we reported on the scheme we have developed for a large angle two-dimensional atom interferometers employing two-photon pulses. The interferometer scheme utilizes Raman pulses to produce a two-dimensional pattern with independent choice of grating spacings in each direction, each being as small as 2 nm. This scheme may enable one to produce uniform arrays of quantum dots with dimensions of only a few nm on each side. Here we report on further theoretical studies thereof, as well as preliminary experimental observations of a robust atom interferometer.

In recent years, rapid progress has been made in the area of atom interferometry. Sensitivity of the modern atomic beam gyroscopes is exceeding that of ring laser gyroscopes[1,2]. Atom interferometers have been used to precisely measure the ratio of Planck's constant to atomic mass, acceleration due to gravity, as well as the gradient thereof[3,4]. Rotation sensors based on atom interferometry may enable measurement of general relativistic Lens-Thirring rotation in the near future. For nano-technology an atom interferometer with a high coherence-length source of atoms, such as the Bose-condensed atom laser[5], would enable the creation of one- and two-dimensional structures with feature sizes of less than 10 nm. For both scientific and technological applications, the sensitivity of an atom interferometer is proportional to the area enclosed by the different paths, which in turn is determined by the degree of splitting at the input port. For the current schemes, the achievable splitting is limited to a few photon recoils. To further increase sensitivity of an atom interferometer, much larger splitting angle is required.

Several schemes of large angle atom cloud splitters have been studied. The interaction of a two level atom with a standing wave light field can produce large splitting angles, but the atoms are scattered into multiple orders[6] because of the sinusoidal nature of the phase grating. The magneto-optic beam-splitter[7-9] and variations thereof[10,11] produce a triangular phase grating, which represents an improvement over the pure standing wave. However, the number of higher orders is still significant because of the sub-wavelength extent of the triangular shapes. In addition, all of these schemes involve an optical interaction with the excited state of the atom and, therefore, suffer from the decoherence effects. In order to minimize these effects, the interaction time has to be small compared to the natural lifetime. This in turn limits the maximum coherent splitting to less than 20 photon recoils due to constraints imposed by high frequency modulators.

Here, we report first detailed analytical studies of our proposed atom beam splitter which can achieve a splitting exceeding $\pm$100 photon recoils. Using the same approach the atom beam or cloud can be recombined easily to yield a high-sensitivity two-dimensional interferometer. The ability of the scheme to generate real two-dimensional interference patterns might be used for lithographic applications such as production of arrays of quantum dots. As an example, we consider the ^{87}Rb atom, released from an evaporatively cooled magnetic trap (or a Bose condensate) and falling under gravity. The relevant energy levels are shown in Figure 1. The atoms are assumed to be in state $|F=1, m_f=1\rangle$ at the onset. We excite the Raman transition, coupling $|F=1, m_f=1\rangle$ (hereafter referred to as $|a\rangle$) to $|F=2, m_f=1\rangle$ (hereafter referred to as $|c\rangle$). The beams are detuned strongly from the excited manifold of the D_2 line, but are two-photon-resonant, so that the process can be thought of as a two-level transition between the two magnetic sublevels. Here, the quantization direction, **z**, is assumed to be normal to the direction of gravity, denoted as **y**.

We assume that right after the atoms are released from their trap, they are in state |a, p_z=0,p_x=0>≡|a,0,0>. We apply two σ_+-polarized beams which are counter-propagating along the **z** axis, with frequencies chosen so one beam (hereafter called A) couples |a> to the excited state, while the other beam (hereafter called C) couples |c> to the same excited state. Both beams are pulsed, with pulse timing chosen so that counter-propagating pulses arrive at the atom simultaneously and leave the atom simultaneously. In our scheme, the first pulse's duration is chosen so that the pulse is a $\pi/2$ pulse, with beam A propagating in the –**z** direction and beam C propagating in the +**z** direction, so that the effect is to place the atom in an equal superposition of |a,0,0> and |c,-2 k,0>. This is illustrated in Figure 2 (solid line transitions). The second pulse pair has a longer duration, chosen so that the pulse is a π pulse, and also has the directions of beams A and C exchanged. This will cause a π-pulse transition between states |a> and |c>, and the reversal of the beam direction will transfer |a,0,0> to |c,+2 k,0> and |c,-2 k,0> to |a,-4 k,0> (dashed-line transitions in Figure 2). Note that the pulses excite two Raman transitions in parallel, that momentum selection rules ensure that there is no mixing of these transitions, and that the atoms are still in an equal superposition of two states. The third pulse pair has the same duration as the second (i.e., it excites a π-pulse transition), but the directions of A and C are again exchanged. The state of the atom after this second π-pulse will now be an equal superposition of |a,+4 k,0> and |c,-6 k,0> (dotted-line transitions in Figure 2). Each subsequent pair of π-pulses again exchanges the directions of A and C, driving the atomic superposition to larger momentum splittings. Inspection of Figure 2 shows that the rule is that the π-pulse traveling in the +**z** direction should have the frequency that interacts with the current atomic state of the +**z**-traveling part of the atoms. After exposure to an even number N_z of these alternating-direction pairs of π-pulses, the atoms will be in an equal superposition of states |a, +2N_z k, 0> and |c, –(2N_z+2) k, 0>.

For example, N_z=24 alternating π-pulses will put the atoms in a superposition of states |a, +48 k,0> and |c, -50 k,0>. The p_z difference of 98 k corresponds to a velocity of about 0.6 m/s, and after 3.3 ms the atoms will separate into two clouds with spatial separation of 2 mm. We can now reverse the motion of the clouds by reversing the splitting scheme—choose the pulse directions so that the –**z**-traveling pulse has the frequency that interact with the +**z**-traveling atoms, and then continue to exchange pulse directions each time a π-pulse exchanges the atomic states. N_z=24 of these reversed pulses would bring the atoms back to the equal superposition of |a,0,0> and |c,-2 k,0>, and a further 25 pulses (for a total of 49) would put the atoms in a superposition of states |c, -50 k, 0> and |a, +48 k, 0>, moving the two halves of the cloud back towards each other.

While the spatially separated components of the superposition state are moving toward each other, we can apply a pair of linearly polarized beams, co-propagating along the **x** direction, causing a Raman transition between |a> and |c> (dotted-line transitions in Figure 1). The duration of this pulse pair is chosen such that a π-pulse is induced on the two-photon transition coupling |a> and |c>, and the location of the beam is chosen so that it only affects the component of the cloud that corresponds to the state |c,-50 k,0>. The atom is now in an equal superposition of the states |a,-50 k,0> and |a,+48 k,0>, since the co-propagating fields give no net momentum transfer in the **x** direction. If left alone these components will come together in about 3.3 ms and form fringes with a peak to peak spacing of about 8 nm. But before that happens we will split (and later recombine) each component further along the **x** axis. We will use a pair of linearly polarized beams with frequencies A and C, counter-propagating in the **x** direction. In a manner analogous to the **z** directed splitting, we first apply a $\pi/2$ pulse, interacting with both components of the split cloud, which produces an equal superposition of four states: { |a, -50 k,0>, |c, -50 k,-2 k>} separated spatially in the **z** direction from { |a, 48 k,0>, |c, 48 k,-2 k>}. This is followed by a series of N_x direction-alternating π-pulse pairs, producing a set of four states. For even N_x, the states are:

{ |a,-50 k,2N_x k>, |c,-50 k,-(2N_x+2) k>} and { |a,48 k,2N_x k>, |c,48 k,-(2N_x+2) k>}. The two clouds in curly brackets are spatially separate from each other in the **z** direction, while inside each cloud two subclouds will now separate out in the **x** direction, with a velocity of 1.2 m/s if N_x=2N_z=48. Thus, after about 1.7 ms, the separation in the **x** direction will be about 2 mm in each cloud. At this point, 2N_x+1=97 π-pulses will be applied in the **x** direction, with the pulse directions chosen to reverse the momentum splitting in the **x** direction. This will produce an equal superposition of the four states:
{ |a, -50 k,-98 k>, |c, -50 k,96 k>} and { |a, 48 k,-98 k>, |c, 48 k,96 k>}.
When these states merge their interference fringe spacing would be on the order of a few nanometers, which would be difficult to detect by optical grating diffraction. To observe the interference and optimize the amplitude in real time, we could scan the phase of one of the laser pulses and detect the atoms either in state |a> or in state |c>. The population in either state is a function of the optical phase scan. This is the internal state interference and the sensitivity of this interference is independent of the splitting angle.

Finally, after optimizing the internal state interference, a **z** directed pair of copropagating, circularly polarized beams are now used to excite a π transition between |a> and |c>, but located spatially so as to affect only the |c> subcloud of each **z** separated cloud. The separation of 2 mm in the **x** direction makes this selective excitation possible. After this pulse sequence, we have four subclouds, converging toward one another in both **x** and **z** directions, and each in the internal state |a>:
{ |a, -50 k,-98 k>, |a, -50 k,96 k>} and { |a, 48 k,-98 k>, |a, 48 k,96 k>}.
Note that the subclouds are now separated in the **z** direction by 1 mm, and in the **x** direction by 2 mm. Similarly, the speed of convergence in the **z** direction (about 0.6 m/s) is half of the convergence speed in the **x** direction. As such, all four components of the cloud will come together in another 1.7 ms, forming a 2 dimensional matter wave grating pattern. The spacing of these patterns are determined by the values of N_z and N_x: for the rubidium transition wavelength of about 800 nm, the peak-to-peak separation in the **z** direction is approximately 100/N_z nm, and the separation in the **x** direction is 100/N_x nm. For the parameters chosen here, we would have a grating with about 4 nm spacing in the **x** direction, and 8 nm spacing in the **z** direction. Structures as small as 2 nm seem feasible given the source particles' parameters considered here. For lithographic applications, this pattern can be deposited on a substrate coated with self-assembled monolayers of octyltrichlorosilane. Then, the damage induced on this layer can be transferred chemically to an underlying layer of semiconductors or coinage metals[13]. The number of spots, and uniformity of height thereof, are determined largely by the coherence length of the sample. For a Bose condensed source, the coherence length is of the order of 300 μm, so that up to 10^{10} structures can be produced and deposited over an area of 300 μm diameter.

In the discussion above, we considered only the state with zero initial momentum. To see the effect of wave packet evolution on the interference pattern, we start with a Gaussian wave packet and Fourier transform it into momentum space. We take into account the initial momentum in the **x** and **z** directions and average the interference process over the initial wave packet. Figure 3 shows schematically the steps involved in producing the two dimensional beam-splitting and recombining. At point S, right after atoms are released from the trap, assume the initial momentum state is $|\psi_0\rangle$=|a, $p_{ox}\hbar k$, $p_{oz}\hbar k$>. In what follows, we assume that the duration of the interaction with the laser pulses is negligible compared to the free evolution time of the wave-packet. Components of the wave-packet following the four distinct paths S-A-A1-E, S-A-A2-E, S-B-B1-E and S-B-B2-E will accumulate phase factors given by the following expressions:

α=Exp{i(-$\hbar k^2$/2m)t[$(p_{oz}-2N_z-2)^2$ + $(p_{oz}+2N_z)^2$ + $(p_{ox}+2N_x)^2$ + $(p_{ox}-2N_x-2)^2$]},
Here t is the time from S to A or B. At point E, the momentum state becomes:
$|\varphi(p_{ox},p_{oz})\rangle = 1/2\alpha_1$ (|a,(p_{oz}+2N_z-2)$\hbar k$, (p_{ox}-2N_x)$\hbar k$>+ |a, (p_{oz}+2N_z-2)$\hbar k$, (p_{ox}+2N_x-2)$\hbar k$>
+ |a, (p_{oz}-2N_z)$\hbar k$, (p_{ox}-2N_x)$\hbar k$>+ |a, (p_{oz}-2N_z)$\hbar k$, (p_{ox}+2N_x-2)$\hbar k$>)
The whole wave packet is then given by:

$$|\varphi\rangle = \iint dp_{ox}\,dp_{oz}\,\frac{2\delta}{\sqrt{2\pi}}\exp[-\delta^2(p_{ox}^{\ 2}+p_{oz}^{\ 2})k^2]^*\,|\,\varphi(p_{ox},p_{oz})\rangle$$

where δ is the standard deviation of the initial packet. The interference pattern is given by $P(x,z)\equiv\psi(x,z)^*\,\psi(x,z)$, where $\psi(x,z)=\langle a, z, x\,|\varphi\rangle$ is the spatial wave function.
P(x,z)=

$$\frac{4a^2}{2\pi(a^4+\frac{^2k^2}{m^2})}\cos^2[(2N_z+1)kz]\cos^2[(2N_x+1)kx]\exp[-\frac{a^2(\frac{2}{m}kt+z)^2}{2(a^4+\frac{^2t^2}{m})}]\exp[-\frac{a^2(\frac{2}{m}kt+z)^2}{2(a^4+\frac{^2t^2}{m})}]$$

From this, we can see that it is a two dimensional interference pattern with Gaussian envelope.

Figure 4 shows a plot of this pattern for δ=10 nm and t=30 ns as a simple example. The relatively small size of the packet is chosen in order to ensure that both the fringe pattern and the roll-off are easily decipherable in the plot. Of course, as discussed above, the initial wave packet size could be as large as 1 mm. In that case, we will have nearly 10^{10} fringes within the envelope.

As described in the previous report, efforts are underway to demonstrate such an interferometer using an atomic beam. The first step is to demonstrate the smallest splitting version of this interferometer, corresponding to a sequence of $\pi/2$-π-$\pi/2$ pulses. Very recently, we have observed this interference, using a novel scheme which is very robust with respect to light-shifts, optical pumping, cooling, and alignments. Briefly, a highly collimated, thermal atomic beam was used, thus making it unnecessary to perform transverse cooling. Second, a simple optical pumping beam was used to transfer all the atoms to the F=3 hyperfine level of ^{85}Rb atoms. Magnetic sublevel optical pumping was not used; instead, a few Gauss of magnetic field was applied to isolate the m_F=0 sublevel. A pair of acousto-optic modulators were used to produce the pair of frequencies necessary for off-resonant Raman excitation. A cycling transition was used to detect efficiently the atoms in the F=2 hyperfine level via fluorescence gathered by an uncooled photomultiplier tube. Most significantly, we used a *single* counter-propagating Raman excitation zone. *Thus, the $\pi/2$-π-$\pi/2$ sequence was realized without any dark zones in-between. The interference fringe was detected by simply scanning the phase of the last quarter of the single zone, by inserting a scanning glass plate in the beam.* While this approach constraints the area of the interferometer (which is important for rotation sensing), this limitation is of no consequence for lithographic application. The area limitation can be overcome easily if one were to use trapped atoms as the source, since the interaction time will then be much larger even for a single zone.

Figure 4 (top graph) shows a preliminary set of atomic interference fringes observed this way. The amplitude variation of the fringes results from intensity variation as a function of the glass plate angle. This can be easily fixed by using a thicker glass plat operating around near normal incidence conditions. The bottom graph shows the corresponding interference fringes observed from a Michelson interferometer where one arm is passed through the sacnning glass plate. No efforts were made to match the phase scan rate, hence the difference in the periodicity of the two graphs. The next step is to demonstrate a larger angle interferometer by extending this approach.

References

1. T. Gustavson, P. Bouyer, and M. Kasevich, Phys. Rev. Lett. **78**, 2046 (1997).
2. D. Keith, C.Ekstrom, Q. Turchette, and D.E. Pritchard, Phys. Rev. Lett. **66**, 2693 (1991)
3. M.J. Snadden et al., Phys. Rev. Letts. **81**, 971(1998).
4. D.S. Weiss, B.C. Young, and S. Chu, Phys. Rev. Lett. **70**, 2706 (1993).
5. M.R. Andrews et al., Science **275**, 637 (1997).
6. P.L. Gould, G.A. Ruff, and D.E. Pritchard, Phys. Rev. Lett. **56**, 827 (1986).

7. T. Pfau, C.S. Adams, and J. Mlynek, Europhys. Lett. **21**, 439 (1993).
8. T. Pfau et al., Phys. Rev. Lett. **71,** 3427 (1993)
9. U. Janicke and M. Wilkens, Phys. Rev. A. **50**, 3265 (1994).
10. P.R. Hemmer, M.S. Shahriar, M.G. Prentiss, D.P. Katz, K. Berggren, J. Mervis, and N.P. Bigelow, Phys. Rev. Lett. **68**, 3148 (1992).
11. K.S. Johnson, A. Chu, T.W. Lynn, K.K. Berggren, M.S. Shahriar, and M. Prentiss, Opt. Letts. **20**, 1310(1995).
12. R. Grimm, J. Soding, and Yu.B. Ovchinnikov, Opt. Lett. **19**, 658(1994).
13. R. Younkin et al. Appl. Phys. Lett. **71,** 1261 (1997).

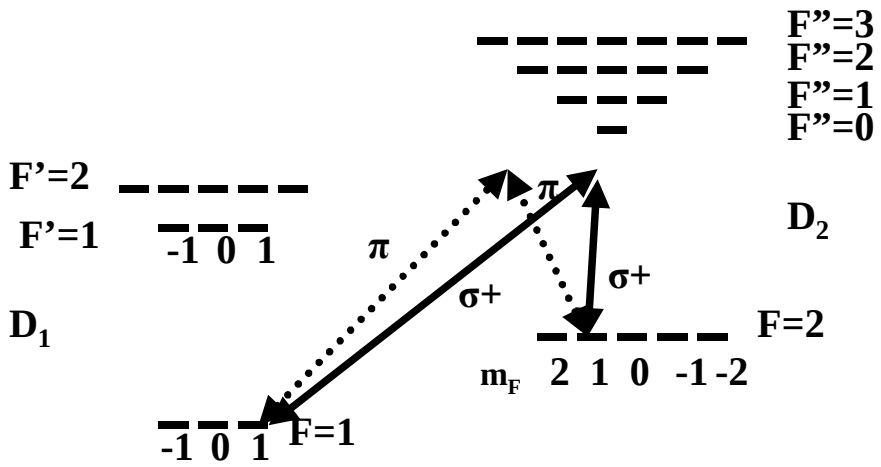

Figure 1. The relevant energy levels of ^{87}Rb atoms (not to scale). Transitions from the D_2 manifolds are used. The presence of two different types of Raman transitions in the D_2 manifold, excitable by optical beams propagating in orthogonal direction, is a key element of this design. Note that because of the particular magnetic sublevels chosen as |a> and |c>, both σ_+ - σ as well as π-π Raman transition exist for coupling these two states. This, for example, is not the case if m_f=0 levels were chosen for both |a> and |c>, because of selection rules prohibiting Δf=0, Δm_f=0 transitions, and the constraint that $|\Delta f| \leq 1$.

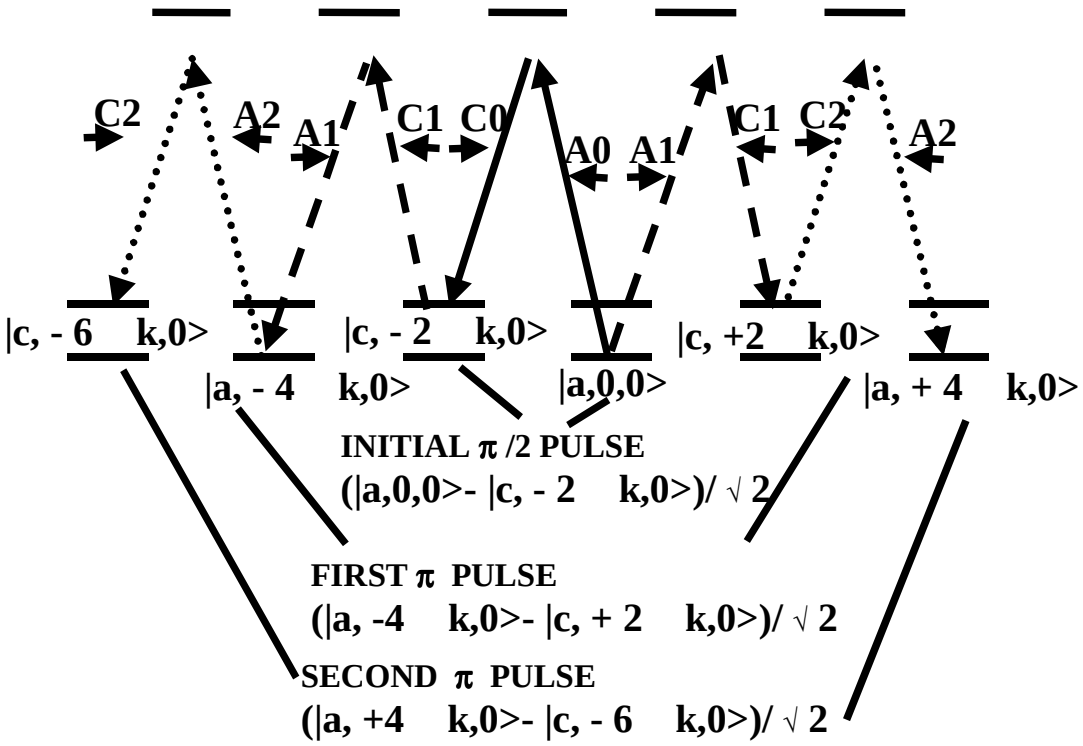

Figure 2. Schematic illustration of the first three pulses in the Raman pulse beamsplitter. Explicit form of the initial superposition state, after excitation with the π/2 pulse, is shown along with the superposition states resulting after the first and second π pulses are applied. Solid lines denote transitions excited with the π/2 pulse, dashed lines denote the first π pulse, dotted lines denote the second π pulse. Note that the π pulses excite two Raman transitions in parallel. Momentum selection rules ensure that there is no mixing of these transitions. For clarity, the energy shifts due to kinetic energy are omitted.

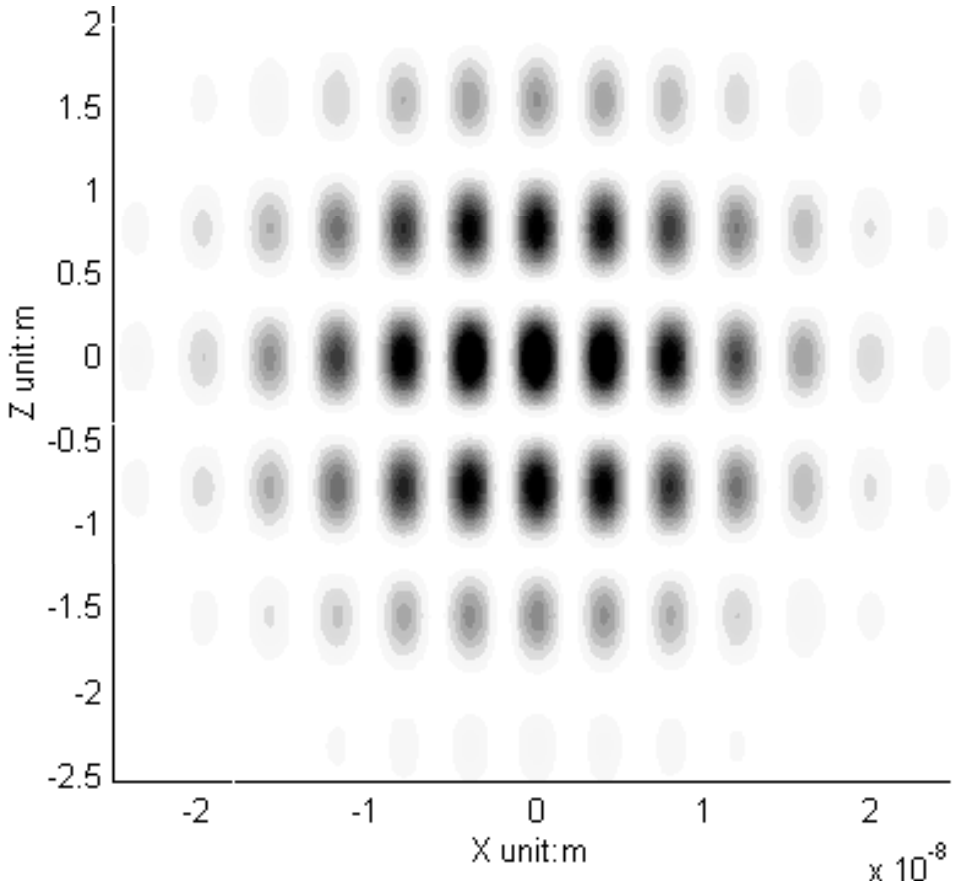

Figure 3. A two-dimensional interference pattern after initial momentum averaging. This simulation assumes a 10 nm initial Gaussian wave packet size and total 60 ns propagation time.

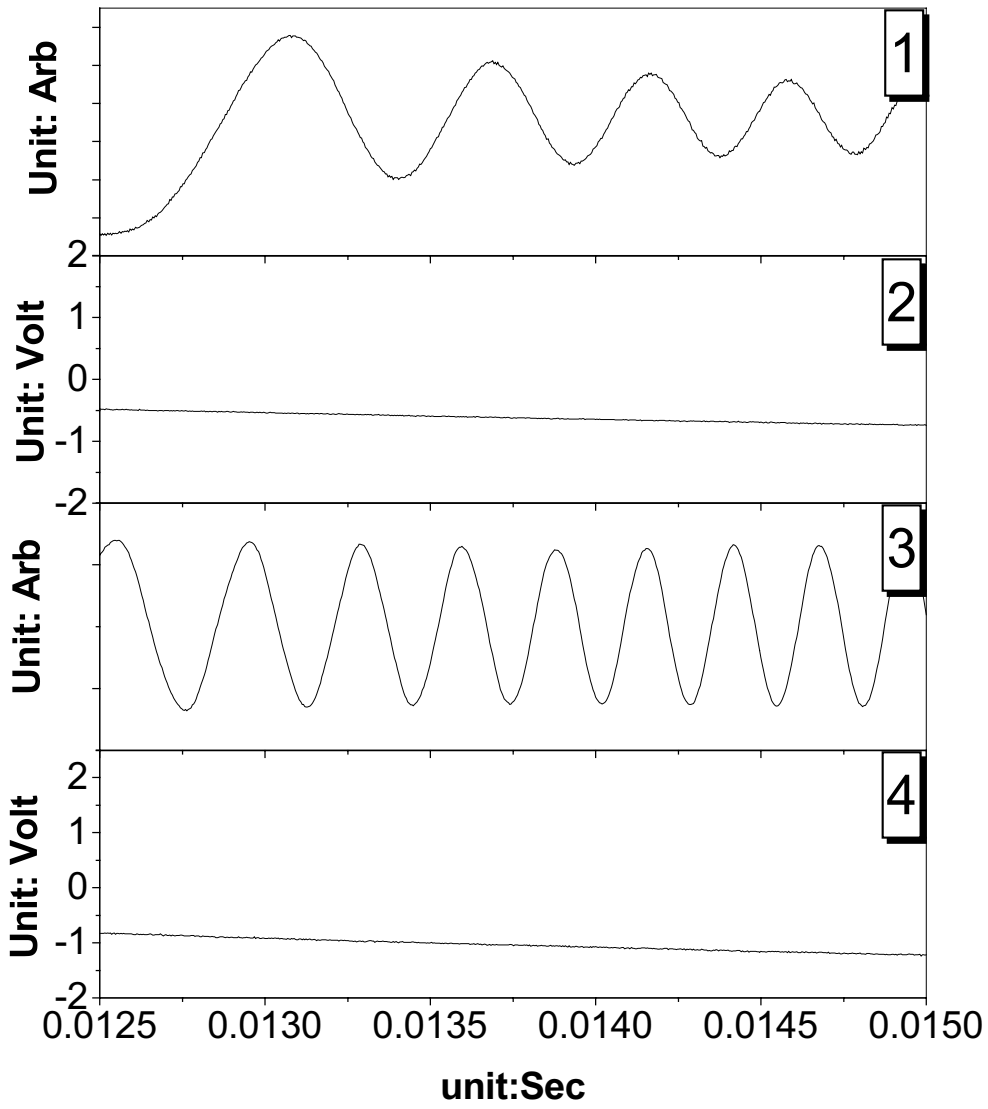

Figure 4. Preliminary set of atomic interference fringes (top graph) observed using the robust scheme described in the text. The amplitude variation of the fringes results from intensity variation as a function of the glass plate angle. This can be easily fixed by using a thicker glass plat operating around near normal incidence conditions. The bottom graph shows the corresponding interference fringes observed from a Michelson interferometer where one arm is passed through the sacnning glass plate. No efforts were made to match the phase scan rate, hence the difference in the periodicity of the two graphs.

4. Long-Distance, Unconditional Quantum Teleportation of a Massive Particle via Complete Measurement of Bell States: Experimental Progress

Sponsor
ARO Grant # DAAD19-001-0177

Previously, we reported on a model we have developed for realizing quantum teleportation of a massive particle via complete measurement of Bell states using ^{87}Rb atoms. Here report our recent experimental efforts towards realizing this goal.

We recall briefly our proposed scheme for constructing a quantum network[1]. The method we developed creates entanglement between two distant atoms using entangled photons. These atoms can exchange quantum information by the process of teleportation[2]. Quantum information processing need only be performed locally. The scheme should allow reliable transmission of quantum information between quantum microcomputers separated by distances of tens of kilometers, without using entanglement purification or quantum error correction[3,4].

In general, it is difficult to create a quantum wire[5]. Direct quantum communication is fragile; existing methods for coping with noisy quantum channels are complicated and time consuming[6]. The solution is to create a quantum network that does not require reliable quantum wires[7]. Cavity quantum electrodynamics provides mechanisms for communicating between cavities [1,7]. The key technology proposed here is a method for transmitting entanglement over long distances, capturing it in optical cavities, and storing it in atoms.

We describe the method in general terms. First, use parametric down conversion to create pairs of momentum- and polarization-entangled photons, sending one to cavity 1 and the other to cavity 2, which are equidistant from the source. Each cavity contains an atom, trapped in an optical potential. Because of their momentum entanglement, each of the entangled pair of photons arrives at its respective cavity at the same time. Although many of the photon pairs will fail to arrive at and enter their respective cavities, on occasion a photon will enter cavity 1 and its entangled pair photon will enter cavity 2 at the same time. Once in the cavity, the photon can drive a transition between the A and the (degenerate) B levels of the atom (figure 1a). This effectively transfers the photon entanglement to the degenerate B levels of the atoms in cavities 1 and 2.

This entanglement can be detected and stored as follows. Concentrate first on a single cavity. To protect the quantum information when the atom has absorbed the photon, drive a transition from B to the long-lived D levels (figure 1a). Now detect if the atom has absorbed a photon by driving a cycling transition from A to C. If no fluorescence is seen, then the atom successfully absorbed the photon and the resulting entanglement in D will be stored for subsequent manipulations. Otherwise, the atom was still in A, which means it failed to absorb the photon. In this case the atom will return to A, ready to absorb the ext photon entering the cavity. When the keeper of cavity 1 has captured a photon, she calls the keeper of cavity 2 to see whether he has captured a photon at the same time. If not, she returns her atom to A and tries again. If both cavities have captured a photon at the same time, however, they now possess two entangled distant atoms.

Let us now look at how such a scheme might be carried out using rubidium atoms (figure 1b). A UV laser will be used to excite a non-linear crystal. Via type-II parametric down-conversion, this crystal will produce pairs of entangled photons, each at 795 nm. An ultrabright, narrow-band parametric amplifier version of this source is described in ref.[8]. We consider the polarization entanglement to be of the form $(|\sigma_+\rangle_1|\sigma\rangle_2+\exp(i\kappa)\ |\sigma\rangle_1|\sigma_+\rangle_2)/\sqrt{2}$, where $\sigma_+(\sigma)$ indicates right(left) circular polarization. The protocol will work for any known value of κ. Each beam is coupled into a fiber, and transported to an optical cavity with slow decay and a strong vacuum Rabi frequency (20 MHz)[9].

Each cavity holds a rubidium atom, confined by a focused CO_2 laser. The mean number of atoms caught is controlled via the parameters involved in the process, and can be reduced to one in a controlled fashion**.** It has been demonstrated recently[10] that at a pressure of 10^{-11} Torr, atoms survive for more than 2 minutes in a CO_2 trap. The trap lifetime may be increased up to an hour by housing the trap chamber in a liquid helium cryostat. In practice, other processes such as fluctuations in the residual magnetic field will limit the decoherence time to a few minutes.

Figure 2 illustrates the transitions to be employed in each cavity. Initially, the atom(s) are prepared in the F=1, m_F=0 ground state (`A' level). The photon excites the dashed transitions to the F=1, $m_F$=±1 excited level (`B' levels) (fig 2a). A π polarized beam completes the Raman excitation, producing a superposition of the F=2, m_F=±1 states ('D' levels). To determine if the photon has been absorbed by the atom, the F=1 state is detected by exciting the cycling transition ('A to C') shown in figure 2b.

The dual-OPA source of ref [8] is capable of producing ~10^6 entangled pairs/sec at 795 nm in ~30 MHz bandwidth. For long-distance transmission, one can generate ~10^6 pairs/sec in the 1550 nm low-loss fiber transmission window. After fiber propagation we can shift the entanglement to the 795 nm via quantum-state frequency translation, previously demonstrated by Kumar[12].The entanglement produced this way can be used for quantum teleportation, quantum cryptography, or remote phase measurement[13], for example. Previously, we have reported an explicit construction for performing the teleportation of a quantum state.

Efforts are underway to realize the the various aspects of this scheme. In particular, our group has been concentrating first on trapping a single atom inside a high finesse optical cavity. Figure 3 shows schematically the basic apparatus we have constructed for trapping a single atom inside a high finesse optical cavity. The bottom chamber houses a magneto-optic trap, loaded from a chirp-slowed atomic beam (not shown, separated via differential pumping). The top chamber is designed to hold the optical cavity. Atoms launched from the bottom chamber via an atomic fountain will enter the top chamber and come to rest at the center of the optical cavity, and then trapped by an off-resonant dipole-force field.

The Fabry-Perot cavity has been constructed using a pair of super-mirrors custom-made by Research Electro Optics Inc. of Boulder, Colorado. We have observed a Q of $2X10^5$. A typical ultra-narrow resonance of this cavity is shown in the top graph of figure 4. In order to stabilize this cavity, we have employed the well-known technique of FM locking, wherein FM sidebands detected in reflection from the cavity is used to generate the error signal. A typical trace of the FM sidebands are shown in the bottom trace of figure 4. The next step is to optimize the fountain, to be followed by trapping of a single atom at the center of the optical cavity by using a focused CO_2 laser beam.

References:

1. J. Cirac et al., *Phys. Rev. Lett.*, **78**, p. 3221 (1997).
2. C. Bennett et.al., *Phys. Rev. Lett.*, **70**, p. 1895 (1993).
3. P. Shor, *Proceedings of the 37th Annual Symposium on the Foundations of Computer Science*, IEEE Computer Society Press, Los Alamitos, p. 56 (1996); D. DiVincenzo and P. Shor, *Phys. Rev. Lett.*, **77**, p. 3260 (1996).
4. P. Shor, *Phys. Rev. A*, **52**, pp. R2493-R2496 (1995); A. Steane, *Phys. Rev. Lett.*, **77**, pp. 793-797 (1996); A. Calderbank and P. Shor, *Phys. Rev. A*, **54**, pp. 1098-1106 (1996); R. Laflamme, C. Miquel, J. Paz, W. Zurek, *Phys. Rev. Lett.*, **77**, p. 198(1996); E. Knill and R. Laflamme, *Phys. Rev. A*, **55**, p. 900 (1997); C. Bennett et. al., *Phys. Rev. A*, **54**, p. 3824 (1996).
5. S. Lloyd, *Science*, **261**, p. 1569 (1993).
6. C. Bennett, D.DiVincenzo, J.Smolin, *Phys. Rev. Lett.*, **78**, p. 3217 (1997); B. Schumacher and M. Nielsen, *Phys. Rev. A*, **54**, p. 2629 (1996); B. Schumacher,

Phys. Rev. A, **54**, p. 2614 (1996); S. Lloyd, *Phys. Rev. A*, **55**, p.1613 (1997).
7. S. van Enk, J. Cirac, P. Zoller, *Phys. Rev. Lett.*, **78**, p. 4293 (1997)
8. J.H. Shapiro and N.C. Wong, J. Opt. B.: Quantum Semiclass. Opt. **2**, L1(2000).
9. S. Morin, C. Yu, and T. Mossberg , *Phys. Rev. Lett.* **73**, p.1489 (1994).
10. K. O'Hara et. al., *Phys. Rev. Lett.* **82**, p. 4204 (1999).
11. J.H. Shapiro, in *Proc. Fifth International Conf. On Quantum Communication, Measurement, and Computing*, Capri 2000, edited by O. Hirota and P. Tombesi, and references therein; also available at *http://xxx.lanl.gov/ps/quant-ph/0105055.*
12. J.M.Huang and P.Kumar,Observation of quantum frequency conversion, *Phys. Rev. Lett.* **68**, 2153 (1992).
13. M.S. Shahriar, *http://xxx.lanl.gov/pdf/quant-ph/001007*
14. T. Pellizzari et. al., *Phys. Rev. Lett.*, **75**, p. 3788 (1995).

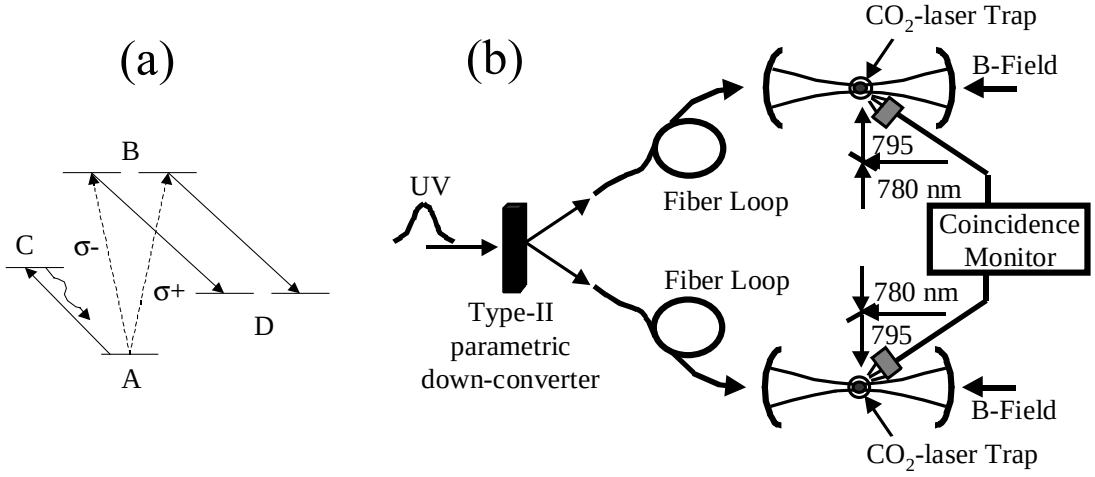

Figure 1. Schematic illustration of the proposed experiment for creating potentially long distance entanglement between a pair of trapped rubidium atoms (see text)

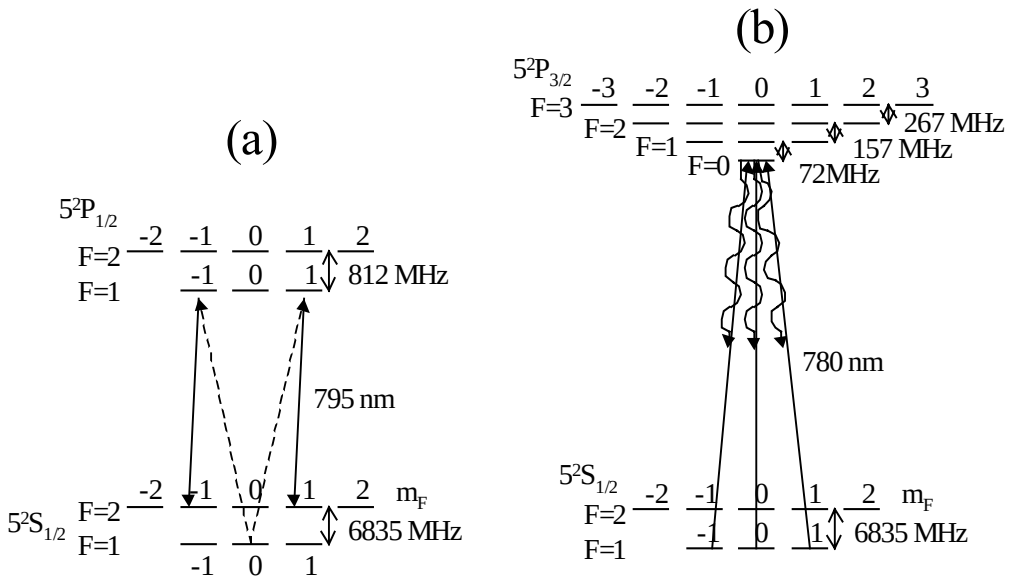

Figure 2. Schematic illustration of the steps to be used in storing quantum coherence in a rubidium atom, and detecting it non-destructively (see text).

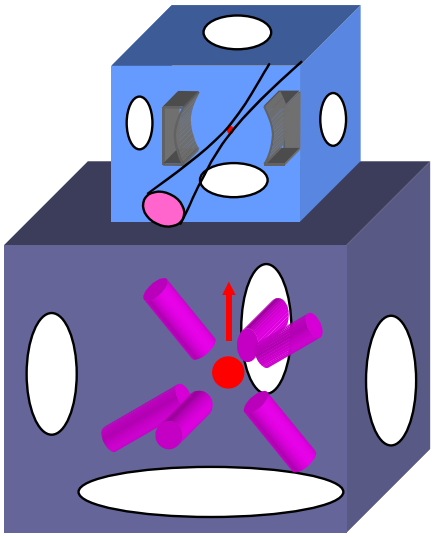

Figure 3. Schematic illustration of the apparatus we have constructed for trapping a single atom inside a high finesse optical cavity. The bottom chamber houses a magneto-optic trap, loaded from a chirp-slowed atomic beam (not shown, separated via differential pumping). The top chamber is designed to hold the optical cavity. Atoms launched from the bottom chamber via an atomic fountain will enter the top chamber and come to rest at the center of the optical cavity, and then trapped by an off-resonant dipole-force field.

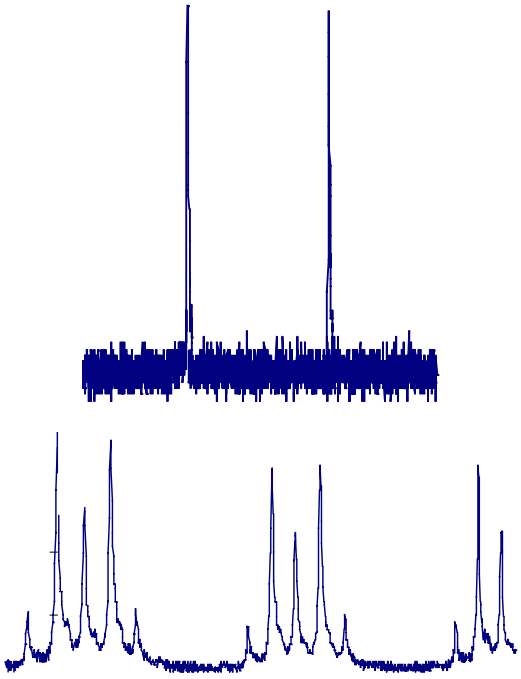

Figure 4. Top: ultra-narrow resonances from the high-finesse cavity, with a measured Q of $2X10^5$. The traces are broadened here by the scope time-constant used to capture the trace.

Bottom: sidebands generated by an electro-optic modulator. These sidebands are used to stabilize the cavity via the FM-locking technique.

5. Remote Phase Measurement via Bloch-Siegert Oscillation and Quantum Teleportation, with Potential Application to Clock Synchronization

Sponsors
AFOSR grant # F49620-98-1-0313, ARO grant #s DAAG55-98-1-0375 and DAAD19-001-0177, and NRO grant # NRO-000-00-C-0158.

A recent proposal[1] by Jozsa et al. to synchronize remote clocks is incomplete because no prescription exists for creating the required prior non-degenerate entanglement, given that the relative phase between the two clocks is unknown. We show how a degenerate entanglement, created without this phase information[2], can be used to determine the relative phase between the remote clocks, via the interference between the co- and counter-rotating excitations of a two-level atom. As such, the protocol offered here achieves the goal of phase-locking remote clocks via transmitting the phase of an oscillator via quantum teleportation.

The proposal[1] by Jozsa et al.[1] shows that if one has a singlet state of two atoms (consisting of entangled states of different but known energy), the intrinsic entanglement of the singlet can be used to create synchronized clocks which can be *simultaneously* started by making a measurement on one of the atoms. This is an important and interesting observation; however, all known methods for constructing a singlet state of two atoms using states of different energy require synchronized clocks to begin with. To put it differently, the challenge of quantum clock synchronization can be reduced to the task of determining the phase difference between two remote clocks. This would enable phase-locking of clocks for applications in VLBI (very large base interferometry)[3]. Here, we report a way to transmit the phase of an oscillator via quantum teleportation.

In order to explain the basic premise of the scheme we are proposing, it is instructive to discuss briefly the physical reason behind the inadequacy of the Jozsa protocol. As is well known, the amplitude of an atomic state is necessarily complex. Whenever a measurement is made, the square of the absolute value of the amplitude is what we can observe. The timing signal from a clock (as represented, e.g., by the amplitude of the magnetic field of an rf oscillator locked to the clock transition), on the other hand, is *real,* composed of the sum of two complex components. In describing the atom-field interaction, one often side-steps this difference by making what is called the *rotating wave approximation* (RWA), under which only one of the two complex components is kept. As a result, generally an atom interacting with a field enables one to measure only the intensity --- and not the amplitude and the phase--- of the field. This is the reason why most detectors are so-called square-law detectors. To see how this affects the Jozsa scheme, note that in essence this protocol attempts to teleport directly the information about the field from one clock to the other location via entanglement. However, because of this square-law effect, which shows up during the measurement/collapse stage of teleportation, what gets teleported is always the intensity, and not the amplitude and the phase. The protocol is thus constrained by the fact that the intensity is a constant, and does not contain any timing information.

This gives us some hints as to how one might solve the problem. Basically, one must modify the atom-field interaction in a way so as to enable the measurement of amplitude and phase of the field. This can be done via what is known as heterodyne detection, an example of which occurs in experiments involving quadrature squeezing. In such an experiment, the weak squeezed field is *multiplied* by a strong field (local oscillator: LO). An atom (or a semiconductor), acting still under the *square-law* limit, can detect this *multiplied* signal, which varies with the phase difference between the weak field and the LO. One can try to use the same idea to modify the

Jozsa protocol. Briefly, one can use two different frequencies to interact simultaneously with the atom. If one of these frequencies corresponded to a clock that was already synchronized with the corresponding clock on the other side, then this method indeed works. However, this is only *shifting* the burden of synchronization, not solving it, as discussed in detail in ref. 4.
Here we show how to circumvent this constarint, by making use of the fact that the two complex parts of the clock field have exactly equal but opposite frequencies (one frequency is the negative of the other), and have exactly correlated phases. By using the so called counter-rotating complex field (which is normally ignored as discussed above) as the LO, we can now measure the amplitude and the phase of the electric field. When this concept is applied to the basic apparatus of the Jozsa protocol, the result is that one is able to teleport the amplitude and the phase of the clock field, thus achieving synchronization.

In our model two observers, Alice and Bob, assumed to be in the same reference frame, have each an atomic clock, which are operating at the same frequency. The relative phase, Ω, between them is unknown to both of them. The basic task is for Alice and Bob both to determine what the value of Ω is. It is clear that classically this can not be established without either Bob or Alice sending the other a sample of his/her oscillating field directly. For example, the rf signal can be encoded as the beat between two optical frequencies, which in turn can be transmitted by laser. However, one must know the optical path length between Bob and Alice; potential variation in optical density (and thus index) of the intervening medium makes it difficult to determine this accurately. This problem lies at the heart of the current approaches used for clock synchronization[5]. Here we show how Ω can be determined without transmitting a timing signal between Alice and Bob, thereby avoiding this problem.

We assume that Alice and Bob each has an atom that has two degenerate ground states (|1> and |2>), each of which is coupled to a higher energy state (|3>), as shown in figure 1. We assume the 1-3 and 2-3 transitions are magnetic dipolar, and orthogonal to each other, with a transition frequency ω. For example, in the case of ^{87}Rb, |1> and |2> correspond to $5^2P_{1/2}$:|F=1,m_F=-1> and $5^2P_{1/2}$:|F=1,m_F=1> magnetic sublevels, respectively, and |3> corresponds to $5^2P_{1/2}$:|F=2,m_F=0> magnetic sublevel. Left and right circularly polarized magnetic fields, perpendicular to the quantization axis, are used to excite the 1-3 and 2-3 transitions, respectively. The rubidium clock is typically stabilized with respect to the $5^2P_{1/2}$:|F=1,m_F=0> to $5^2P_{1/2}$:|F=2,m_F=0> transition, which is excited by a magnetic field parallel to the quantization axis[6]. We take ω to be the same as the clock frequency ω_c.

We assume that Alice and Bob's fields at ω have the form $B_A=B_{ao}Cos(\omega t+\phi)$ and $B_B=B_{bo}Cos(\omega t+\chi)$, respectively. The origin of the time variable, t, is therefore arbitrary, and does not affect the quantity of interest: the phase difference, $\Omega\equiv(\phi-\chi)$. The clocks are assumed to be in phase if Ω=0, so that if Bob determines that at some instant his magnetic field is maximum and positive in some direction $\boldsymbol{r}_b$, then Alice will also find her magnetic field to be maximum and positive in some direction $\boldsymbol{r}_a$ at the same instant. As long as Alice and Bob agree on this definition of phase-locking, and use the same definitions all the time, then $\boldsymbol{r}_b$ and $\boldsymbol{r}_a$ do not have to be the same. During the magnetic resonance excitations, the value of any dc magnetic field will be assumed to be vanishing. Symmetry then dictates that any physical observable will be independent of the choice of the quantization axis, as long as it is perpendicular to $\boldsymbol{r}_a$ for Alice, and perpendicular to $\boldsymbol{r}_b$ for Bob. Before we discuss our protocol, we summarize briefly a two-level interaction *without* RWA, and time reversal of an arbitrary evolution under this condition.

Consider, for example, the excitation of the $|1\rangle_A \leftrightarrow |3\rangle_A$ transition. In the dipole approximation, the Hamiltonian can be written as:

$$\hat{H} = \begin{bmatrix} 0 & g(t) \\ g(t) & \varepsilon \end{bmatrix} \qquad \ldots(1)$$

and the state vector is written as:

$$|\xi(t)\rangle = \begin{bmatrix} C_{1A} \\ C_{3A} \end{bmatrix} \quad \ldots(2)$$

where $g(t) = -g_o[\exp(i\omega t+i\phi)+c.c.]/2$, and we assume that $\varepsilon=\omega$ corresponding to resonant excitation. Here, we have assumed that the polarization of Alice's field can be changed to excite either $|1\rangle_A \leftrightarrow |3\rangle_A$ or the $|2\rangle_A \leftrightarrow |3\rangle_A$ transition, in a mutually exclusive manner. We now perform a rotating wave transformation by operating on $|\xi(t)\rangle$ with the unitary operator Q, given by:

$$\hat{Q} = \begin{bmatrix} 1 & 0 \\ 0 & \exp(i\omega t + i\phi) \end{bmatrix} \quad \ldots(3)$$

The Schroedinger equation then takes the form (setting $\hbar$=1):

$$\frac{\partial |\tilde{\xi}(t)>}{\partial t} = -i\tilde{H}(t)|\tilde{\xi}(t)> \quad \ldots.(4)$$

where the effective Hamiltonian is given by:

$$\tilde{H} = \begin{bmatrix} 0 & \alpha(t) \\ \alpha^*(t) & 0 \end{bmatrix} \quad \ldots(5)$$

with $\alpha(t)= -g_o[\exp(-i2\omega t-i2\phi)+1]/2$, and the rotating frame state vector is:

$$|\tilde{\xi}(t)> \equiv \hat{Q}|\tilde{\xi}(t)> = \begin{bmatrix} \tilde{C}_{1A} \\ \tilde{C}_{3A} \end{bmatrix} \quad \ldots(6)$$

At this point, one may choose to make the rotating wave approximation (RWA), corresponding to dropping the fast oscillating term in $\alpha(t)$. As we will show, this corresponds to ignoring effects (such as the Bloch-Siegert shift) of the order of (g_o/ω), which can easily be observable if g_o is large[7-10]. On the other hand, by choosing g_o to be small enough, we can make the RWA for any value of ω We will make use of both regimes in our protocol. As such, we will now find the results without the RWA.

Given the periodic nature of the effective Hamiltonian, the general solution to eqn. 5 can be written as:

$$|\tilde{\xi}(t)> = \sum_{n=-\infty}^{\infty} |\xi_n\rangle \beta^n \quad \ldots(7)$$

where $\beta=\exp(-i2\omega t-i2\phi)$, and

$$|\xi_n\rangle \equiv \begin{bmatrix} a_n \\ b_n \end{bmatrix} \quad \ldots(8)$$

Inserting eqn. 7 in eqn. 4, and equating coefficients with same frequencies, we get, for all n:

$$\begin{aligned} \dot{a}_n &= i2n\omega a_n + ig_o(b_n + b_{n-1})/2 \\ \dot{b}_n &= i2n\omega b_n + ig_o(a_n + a_{n+1})/2 \end{aligned} \quad \ldots(9)$$

Figure 2 shows a pictorial representation of these equations. Here, the coupling between a_o and b_o is the conventional one present when the RWA is made. The coupling to additional levels results from virtual multiphoton processes in the absence of the RWA. The couplings to the nearest neighbors, $a_{\pm 1}$ and $b_{\pm 1}$ are detuned by an amount 2ω, and so on. To the lowest order in (g_o/ω), we can ignore terms with $|n|>1$, thus yielding a truncated set of six eqns.:

$$\dot{a}_o = ig_o(b_o + b_{-1})/2 \qquad (10.1)$$

$$\dot{b}_o = ig_o(a_o + a_1)/2 \qquad (10.2)$$

$$\dot{a}_1 = i2\omega a_1 + ig_o(b_1 + b_o)/2 \qquad (10.3)$$

$$\dot{b}_1 = i2\omega b_1 + ig_o a_1/2 \qquad (10.4)$$

$$\dot{a}_{-1} = -i2\omega a_{-1} + ig_o b_{-1}/2 \qquad (10.5)$$

$$\dot{b}_{-1} = -i2\omega b_{-1} + ig_o(a_{-1} + a_o)/2 \qquad (10.6)$$

In order to solve these equations, one may employ the method of adiabatic elimination valid to first order in $\sigma \equiv (g_o/4\omega)$. To see how this can be done, consider first the last two equations: 10.5 and 10.6. In order to simplify these two equations further, one needs to diagonalize the interaction between a_{-1} and b_{-1}. To this end, we define $\mu_- \equiv (a_{-1} - b_{-1})$ and $\mu_+ \equiv (a_{-1} + b_{-1})$, which can be used to re-express these two equations in a symmetric form as:

$$\dot{\mu}_- = -i(2\omega + g_o/2)\mu_- - ig_o a_o/2 \qquad (11)$$

$$\dot{\mu}_+ = -i(2\omega - g_o/2)\mu_+ + ig_o a_o/2 \qquad (12)$$

Adiabatic following then yields (again, to lowest order in σ):

$$\mu_- \approx -c\,a_o; \qquad \mu_+ \approx c\,a_o \qquad (13)$$

which in turn yields:

$$a_{-1} \approx 0; \qquad b_{-1} \approx c\,a_o \qquad (14)$$

In the same manner, we can solve eqns. 10.3 and 10.4, yielding:

$$a_1 \approx -c\,b_o; \qquad b_1 \approx 0 \qquad (15)$$

Note that the amplitudes of a_{-1} and b_1 are vanishing (each proportional to σ^2) to lowest order in σ, thereby justifying our truncation of the infinite set of relations in eqn. 9. Using eqns. 14 and 15 in eqns. 10.1 and 10.2, we get:

$$\dot{a}_o = ig_o b_o/2 + i\Delta a_o/2 \qquad (16)$$

$$\dot{b}_o = ig_o a_o/2 - i\Delta b_o/2 \qquad (17)$$

where $\Delta = g_o^2/4\omega$ is essentially the Bloch-Siegert shift. Eqns. 16 and 17 can be thought of as a two-level system excited by a field detuned by Δ. With the initial condition of all the population in $|1\rangle_A$ at t=0, the only non-vanishing (to lowest order in σ) terms in the solution of eqn. 9 are:

$$a_o(t) \approx Cos(g_o t/2); \quad b_o(t) \approx iSin(g_o t/2)$$

$$a_1(t) \approx -i\sigma Sin(g_o t/2); \quad b_{-1}(t) \approx \sigma Cos(g_o t/2) \qquad (18)$$

We have verified this solution via numerical integration of equation 10, as illustrated in figure 3. Inserting this solution in eqn. 7, and reversing the rotating wave transformation, we get the following expressions for the components of eqn. 2:

$$C_{1A}(t) = Cos(g_o t/2) - 2i\sigma\Sigma \cdot Sin(g_o t/2)$$
$$C_{3A}(t) = ie^{-i(\omega t+\phi)}[Sin(g_o t/2) + 2\sigma\Sigma^* \cdot Cos(g_o t/2)] \qquad (19)$$

where we have defined $\Sigma \equiv (i/2)\exp[-i(2\Delta t + 2\phi)]$. To lowest order in σ this solution is normalized at all times. Note that if Alice were to carry this excitation on an ensemble of atoms through for a π/2 pulse, and measure the population of the state $|1\rangle_A$ immediately (at t=τ, the moment when the π/2 excitation ends), the result would be a signal given by

$[1+2\sigma Sin(2\omega\tau+2\phi)]/2$, which contains information related to the amplitude and phase of her field. Next, we consider the issue of exact time reversal of such an excitation. The Schroedinger eqn. (4) has the formal solution:

$$|\tilde{\xi}(t_2)\rangle = \exp(-i\int_{t_1}^{t_2} \tilde{H}(t')dt')\,|\tilde{\xi}(t_1)\rangle \qquad \ldots(20)$$

If the RWA is made, then $\tilde{H}$ is time independent. In that case, if one starts an evolution at t_1, proceed for *any* duration T, then reverses the sign of $\tilde{H}$ by shifting the phase of the magnetic field by π, and continues with the evolution for another duration T, then the system returns back to the starting state. Of course, this can be verified explicitly using the well known solution of Rabi flopping. Here, however, RWA is not made, so that $\tilde{H}$ depends on time. Therefore, the exact reversal can be achieved in this manner only if $T=m\pi/\omega$ for any integer value of m. We have verified this conclusion via numerical integration as well (not shown).

Returning to the task at hand, our protocol starts by using a scheme, developed earlier by us[2](note that this scheme works for ^{87}Rb, for the choice of |1> and |2> indicated above) to produce a degenerate entanglement of the form $|\psi\rangle=(|1\rangle_A|2\rangle_B - |2\rangle_A|1\rangle_B)/\sqrt{2}$. Next, Alice attenuates her field so that the counter-rotating term in the Hamiltonian can be ignored (this assumption is not essential for our conclusion, but merely simplifies the algebra somewhat), and excites a π-pulse coupling $|2\rangle_A$ to $|3\rangle_A$, and then stops the excitation. Similarly, Bob uses a field, attenuated as above, to excite a π-pulse coupling $|2\rangle_B$ to $|3\rangle_B$, and then stops the excitation. Using digital communications over a classical channel, Alice and Bob wait until they both know that these excitations have been completed. The resulting state is then given by :

$$|\psi(t)\rangle=[|1\rangle_A|3\rangle_B\exp(-i\omega t-i\chi) - |3\rangle_A|1\rangle_B\exp(-i\omega t-i\phi)]/\sqrt{2}. \qquad \ldots(21)$$

The next step is for Alice to make a measurement along the $|1\rangle_A \leftrightarrow |3\rangle_A$ transition. For this process, she chooses a much larger value of g_o, so that the RWA can not be made. The state she wants to measure is *the one that would result if one were to start from state $|1\rangle_A$, and evolve the system for a π/2 pulse using this stronger g_o*:

$$|+\rangle_A \equiv \frac{1}{\sqrt{2}}\left[\{1-2\sigma\Sigma\}|1\rangle_A + ie^{-i(\omega t+\phi)}\{1+2\sigma\Sigma^*\}|3\rangle_A\right] \qquad \ldots(22)$$

where we have made use of eqn. 19. The state orthogonal to $|+\rangle_A$ results from a 3π/2 pulse:

$$\left|-\right\rangle_A \equiv \frac{1}{\sqrt{2}}\left[\left\{1+2\sigma\Sigma\right\}\left|1\right\rangle_A - ie^{-i(\omega t+\phi)}\left\{1-2\sigma\Sigma^*\right\}\left|3\right\rangle_A\right] \quad \ldots(23)$$

To first order in σ, these two states are each normalized, and orthogonal to each other. As such, one can re-express the state of the two atoms in eqn. 21 as:

$$\left|\psi(t)\right\rangle = \frac{1}{\sqrt{2}}\left[\left|+\right\rangle_A\left|-\right\rangle_B - \left|-\right\rangle_A\left|+\right\rangle_B\right] \quad \ldots(24)$$

where we have defined:

$$\left|+\right\rangle_B \equiv \frac{1}{\sqrt{2}}\left[\left\{1-2\sigma\Sigma\right\}\left|1\right\rangle_B + ie^{-i(\omega t+\chi)}\left\{1+2\sigma\Sigma^*\right\}\left|3\right\rangle_B\right] \quad \ldots(25)$$

$$\left|-\right\rangle_B \equiv \frac{1}{\sqrt{2}}\left[\left\{1+2\sigma\Sigma\right\}\left|1\right\rangle_B - ie^{-i(\omega t+\chi)}\left\{1-2\sigma\Sigma^*\right\}\left|3\right\rangle_B\right] \quad \ldots(26)$$

She can measure the state $|+>_A$ by taking the following steps: (i) Shift the phase of the B-field by π, (ii) Fine tune the value of g_o so that $g_o=\omega/2m$, for an integer value of m, (iii) apply the field for a duration of $T=\pi/2g_o$, and (iv) detect state $|1>_A$. Note that the constraint on g_o ensures that $T=m\pi/\omega$, which is necessary for time reversal to work in the absence of the RWA. Once Alice performs this measurement, the state for Bob collapses to $|->_B$, given in eqn. 26. Note that if σ is neglected, then the measurement produces a $|->_B$ that contains no information about the phase of Alice's clock, which is analogous to the Jozsa protocol[1].

In the present case, $|->_B$ does contain information about the amplitude and the phase of Alice's clock signal. In order to decipher this, Bob measures his state $|1>_B$, at a time $t=T_B$ so that his B field has the maximum value B_o, which implies that $(\omega T_B+\chi)=2q\pi$, where q is any integer. The probability of success is:

$$p_\phi \equiv \left|{}_B\left\langle 1\right|+\right\rangle_B\Big|^2_{t=T_B} = \frac{1}{2}\left[1+2\sigma Sin(2\Omega)\right]. \quad \ldots(27)$$

where we have kept terms only to the lowest order in σ. *Thus, the whole process is equivalent to remote interferometry without transmitting a timing signal directly*. Note that the signal given by eqn. 27 would be the same even if Bob had not excited $|2>_B$ to $|3>_B$. Of course, the value of Ω (mod 2π), the phase difference, can not be determined from knowing Sin(2Ω) alone. However, this whole process can be repeated after, for example, Alice shifts the phase of her B-field by π/2, so that Bob can determine the value of Cos(2Ω). It is then possible to determine the value of Ω (mod 2π) unambiguously.

The overall process can be carried out in one of two ways. First, consider the situation where Alice and Bob starts with X pairs of atoms, and entangle each pair in the form of equation 24. Then, over a digital communication channel, Alice sends Bob a list of the M atoms she found in state $|1>_A$ after performing her measurement process described above. Bob performs his measurement only on this subset of atoms. Suppose he finds L number of atoms in state $|1>_B$. Then:

$$\eta \equiv \left(\frac{L}{M}-\frac{1}{2}\right) \to \sigma Sin(2\Omega) \qquad \text{, for large } M \quad \ldots(28)$$

Thus, the value of η determined asymptotically for a large number of entangled pairs will reveal the value of Sin(2Ω). Alternatively, if only a single pair of atoms is available, then the same result

can be obtained by repeating the whole process X times, assuming that ϕ remains unchanged during the time needed for the process.

Once the value of $\Omega \pmod{2\pi}$ is determined, Bob can adjust the phase of his clock accordingly, thus achieving phase-locking. This is all that is required for applications such as very large base interferometry[3]. For applications[5] where it is necessary to have a shared origin of time, one can use the method of using two clocks of slightly different frequencies, as proposed in ref.1, assuming that clocks of each type will be synchronized first using the protocol we just presented. Such clocks can be realized, for example, by making use of asymmetric ac-Stark shifts of the $5^2P_{1/2}$:$|F=1,m_F=0\rangle$ and $5^2P_{1/2}$:$|F=2,m_F=0\rangle$ states in the presence of an off-resonant Raman excitation with unbalanced laser intensities[11,12]. Note that such a Raman excitation, which is functionally equivalent (aside from the asymmetric stark shift) to a direct rf excitation, can itself be used as an atomic clock[13,14].

References:

1. R. Jozsa, D.S. Abrams, J.P. Dowling, and C.P. Williams, *Phys. Rev. Letts.* ***85****, 2010(2000).*
2. S.Lloyd, M.S. Shahriar, and P.R. Hemmer, *quant-ph/0003147.*
3. G.S. Levy et al., *Acta Astonaut*. **15**, 481(1987).
4. E.A. Burt, C.R. Ekstrom, and T.B. Swanson, *quant-ph/0007030*
5. National Research Council Staff, *The Global Positioning System: A Shared National Asset*, National Academy Press, Washington, D.C., 1995.
6. A. Corney, Atomic and Laser Spectroscopy, Oxford University Press, 1977.
7. L. Allen and J. Eberly, Optical Resonance and Two Level Atoms, Wiley, 1975.
8. F. Bloch and A.J.F. Siegert, *Phys. Rev.* **57**, 522(1940).
9. J. H. Shirley, *Phys. Rev.* **138,** 8979 (1965).
10. S. Stenholm, *J. Phys. B* 6, (Auguts, 1973).
11. J.E. Thomas et al., *Phys. Rev. Lett*. **48**, 867(1982).
12. P.R. Hemmer, M.S. Shahriar, V. Natoli, and S. Ezekiel, *J. of the Opt. Soc. of Am. B*, **6**, 1519(1989).
13. M.S. Shahriar and P.R. Hemmer, *Phys. Rev. Lett.* **65**, 1865(1990).
14. M.S. Shahriar et al., *Phys. Rev. A*. **55**, 2272 (1997).

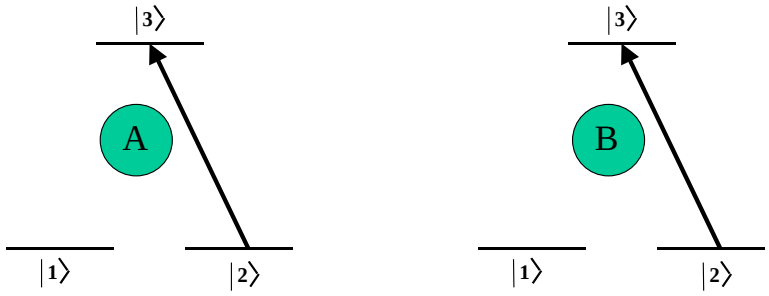

Figure 1. Schematic illustration of the basic protocol for phase locking two remote clocks, one with Alice (A), and the other with Bob (B), without transmitting a clock signal directly. The model energy levels can be realized, for example, using the metastable hyperfine Zeeman sublevels of ^{87}Rb atoms, as detailed in the text.

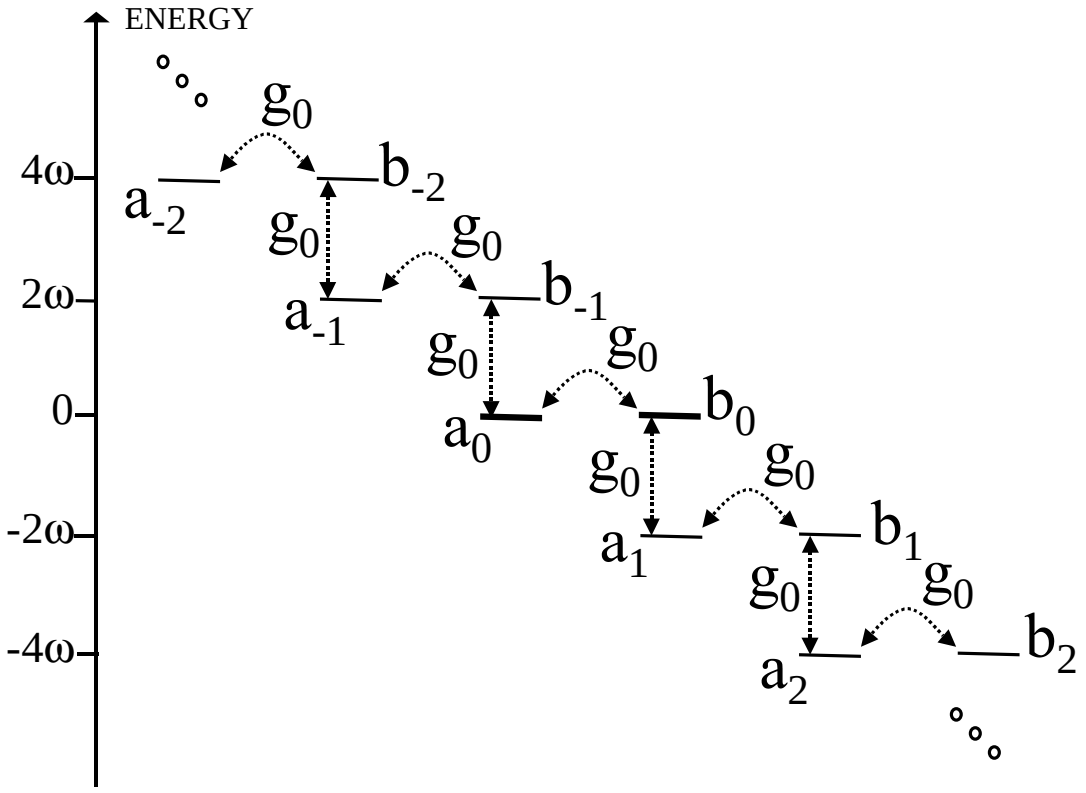

Figure 2. Schematic illustration of the multiple orders of interaction when the rotating wave approximation is not made. The strengths of the first higher order interaction, for example, is weaker than the zeroth order interaction by the ratio of the Rabi frequency, g_o, and the effective detuning, 2ω

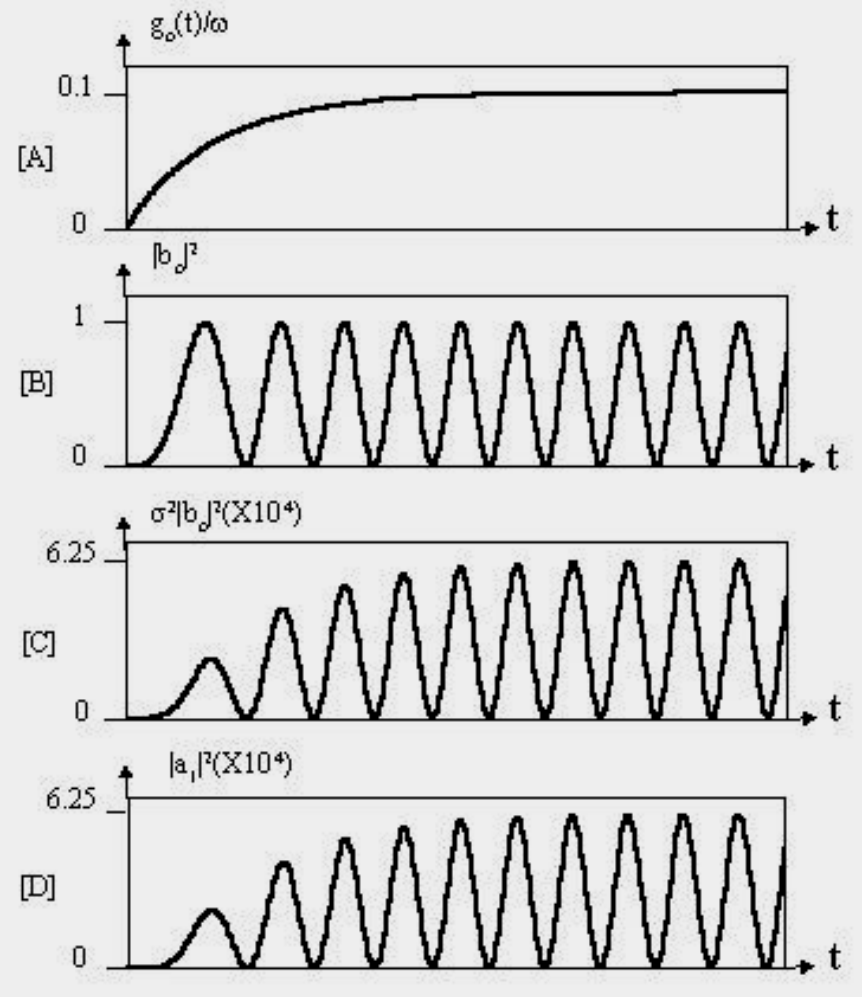

Figure 3. Sample results from numerical integration of eqn. 10, confirming the result obtained analytically via adiabatic following: [A] The rabi frequency g_o as a function of time, normalized to the constant transition frequency, ω The growth of g_o is slow enough to allow for the adiabaticity condition to remain valid. [B] The corresponding evolution of $|b_o|^2$. [C] The value of $\sigma^2|b_o|^2$, which, according to the analytic solution is expected to be the value of $|a_1|^2$. [D] The value of $|a_1|^2$, which is virtually identical to $\sigma^2|b_o|^2$, thus confirming the analytic solution. The other components (e.g. $|b_{-1}|^2$) not shown here also agree with the analytical solution.